

# UniMatSim: A High-Throughput Materials Simulation Automation Framework Based on Universal Machine Learning Potentials

Yanjin Xiang<sup>a</sup>, Yihan Nie<sup>a</sup>, Yunzhi Gao<sup>a</sup>, Haidi Wang<sup>b,\*</sup>, Wei Hu<sup>a,\*</sup>

<sup>a</sup>*School of Emerging Technology, Hefei National Research Center for Physical Sciences at the Microscale, and Hefei National Laboratory, University of Science and Technology of China, Hefei, Anhui 230026, China*

<sup>b</sup>*School of Physics, Hefei University of Technology, Hefei, Anhui 230009, China*

arXiv:2603.15294v1 [cond-mat.mtrl-sci] 11 Mar 2026

## Abstract

The universal machine learning interatomic potentials (UMLIPs) have emerged as a new generation of atomic-scale modeling method, offering accuracy close to first-principles calculations at a fraction of the computational cost, which shows significant potential for large-scale material simulations. However, the current UMLIPs software and toolchain ecosystem remains fragmented, lacking unified interface standards and a standardized framework for integration and workflow scheduling. This severely hinders their large-scale, automated deployment in high-throughput materials simulation workflows. To address this, we present UniMatSim, a Python framework based on unified interfaces and modular design. It is designed to systematically integrate various UMLIPs (e.g., CHGNet, M3GNet, MACE) and to automate the entire workflow from structural optimization and property calculation to stability verification. The framework enables seamless model switching via abstracted computational engine interfaces. It incorporates built-in task registration and workflow orchestration, provides standardized modules for calculating key properties like elasticity, phonons, and molecular dynamics, and includes automated handling for low-dimensional materials. As a test case, using the two-dimensional Lieb lattice system, we constructed a multi-stage high-throughput screening workflow covering structural optimization, elastic stability screening, and phonon spectrum calculation. Starting from 1,176 candidate compositions, a four-model consensus pipeline yields 393 stable structures, which are then refined by magnetic-state screening and DFT band-structure calculations to 59 Lieb-lattice candidates with staggered-magnetic-band characteristics. Results show that UniMatSim offers significant advantages in improving computational efficiency and ensuring reproducibility. Therefore, we present UniMatSim, a unified, efficient, and extensible high-throughput computational framework for universal UMLIPs, providing reliable infrastructure for data-driven materials discovery and design.

**Keywords:** High-throughput calculations, Machine learning interatomic potentials, Materials simulation, Workflow automation

## PROGRAM SUMMARY

*Program Title:* UniMatSim

*CPC Library link to program files:* (to be added by Technical Editor)

*Developer's repository link:* <https://gitee.com/haidi-hfut/unimatsim>

*Licensing provisions:* MIT License

*Programming language:* Python 3.7+

*Nature of problem:* The integration of various universal machine learning interatomic potentials (UMLIPs) into a unified high-throughput screening workflow is currently hindered by fragmented interfaces and the lack of automated scheduling tools.

*Solution method:* We developed UniMatSim, a Python-based framework that provides a unified interface for multiple UMLIPs (CHGNet, M3GNet, MACE, etc.) and integrates an

automated workflow engine for structural relaxation, stability analysis, and property calculation.

## 1. Introduction

Materials science is experiencing a paradigm shift driven by data-driven methodologies[1, 2]. Historically, materials discovery has relied heavily on empirical knowledge and trial-and-error experimentation. This approach is not only time-consuming and costly but also struggles to systematically explore the vast design space defined by composition, structure, and processing. Advances in computational power and theoretical methods have positioned high-throughput computational simulation as a key tool to overcome these limitations[3, 4, 5]. By implementing standardized, automated workflows, it enables the rapid prediction, screening, and ranking of physical, chemical, and functional properties across thousands of candidate materials, compressing the development timeline

\*Corresponding authors.

*E-mail addresses:* haidi@hfut.edu.cn (Haidi Wang)

*E-mail addresses:* whuustc@ustc.edu.cn (Wei Hu)

from years to months or even weeks. This computation-driven, experiment-guided paradigm[6] dramatically reduces the cost and uncertainty associated with early-stage exploration. Its impact is particularly pronounced in critical fields such as energy storage materials[7], semiconductors, industrial catalysts, and structural alloys (e.g., high-entropy alloys)[8, 9], where it unlocks new opportunities for rational, performance-oriented design, offering considerable scientific and strategic value.

In recent years, new-generation machine learning techniques, particularly universal machine learning interatomic potentials (UMLIPs), have advanced rapidly within materials simulation, profoundly reshaping the traditional research paradigm centered on first-principles calculations[10, 11]. For instance, models like CHGNet[12], M3GNet[13], MACE[14], MatterSim[15], and SevenNet[16] deliver accuracy comparable to Density Functional Theory (DFT) while offering computational speedups of several orders of magnitude[13, 12]. This opens new avenues for large-scale screening and dynamic simulations of materials across different scales and compositions. However, integrating these advanced potentials into practical materials research in an efficient, reliable, and scalable manner remains challenging. On one hand, the current ecosystem is fragmented; different models are developed and maintained independently, leading to significant disparities in computational workflows, model loading, parameter configuration, and interfaces for fine-tuning and inference. This lack of a unified abstraction layer and standardized calling conventions[11, 17] increases the overhead for researchers and impedes systematic model comparison, integration, and broader adoption. On the other hand, although workflow management frameworks such as `atome2`[17], `jobflow`[17], and `AiiDA`[18] have emerged and successfully automated traditional DFT calculations, they are primarily designed for first-principles engines and lack a unified interface and agnostic abstraction for the diverse and rapidly evolving landscape of machine learning potentials. [11, 13]. Consequently, there is a pressing need for a unified integration framework dedicated to UMLIPs to enable standardized access, efficient scheduling, and large-scale automated deployment.[11, 16]

To tackle these challenges, we present `UniMatSim`, an integrated Python framework for high-throughput materials simulation. Its design adheres to the principles of unified interfaces, modular decoupling, and extensibility. The framework aims to bridge machine learning potentials with automated materials research, offering a streamlined, efficient, and reliable platform for computational studies. The core innovation is a multi-tiered standardization architecture. At the base level, a unified `PotentialModel` interface encapsulates diverse potentials (e.g., CHGNet, M3GNet, MACE), enabling seamless model switching through simple configuration, eliminating the need to rewrite scripts or adapt calling protocols. At the task level, common simulation steps—including structural optimization, elastic constant calculation, phonon spectrum analysis, and molec-

ular dynamics simulation—are abstracted into standardized, reusable `Task` modules, each with well-defined inputs, outputs, and execution logic. At the workflow level, an intelligent `WorkflowEngine` automates task orchestration, dependency resolution, parallel scheduling, and state management, facilitating the construction of computational pipelines from simple linear sequences to complex directed acyclic graphs (DAGs). Additionally, the framework incorporates specialized features for low-dimensional materials (e.g., automatic dimensionality recognition, in-plane relaxation constraints, 2D Brillouin zone path generation) and a comprehensive stability assessment system covering elastic, dynamical, and thermodynamic properties. Together, these components deliver an end-to-end solution for high-throughput screening, applicable to systems ranging from 3D bulk materials to 2D layered structures. Through this systematic design, `UniMatSim` is engineered to advance the automation, reproducibility, and overall efficiency of materials simulation, allowing researchers to dedicate greater focus to core scientific inquiry rather than computational logistics.

The rest of this work is structured as follows. Section II ("Methods and Implementation") details the overall architecture and key modules of `UniMatSim`. Section III ("Case Study") demonstrates the framework’s complete workflow, computational efficiency, and robustness in practice, using high-throughput stability screening of a two-dimensional Lieb lattice system as a representative example. Finally, Section IV ("Conclusion and Outlook") concludes the paper and discusses future development directions for the framework, such as enhanced integration of machine learning potentials, adaptive workflows, and interactive interfaces.

## 2. System Architecture Design

`UniMatSim` employs a layered, modular architecture consisting of six core hierarchical tiers: the Core Infrastructure Layer (Core), the Structure Manipulation Layer (Structures), the Computational Engine Layer (Engine), the Workflow Management Layer (Workflows), the Data Processing Layer (Data), and the Interface Layer (Interface). The framework adheres to the separation-of-concerns principle. Interactions between layers are facilitated through well-defined interfaces, enabling the independent development, testing, and maintenance of individual modules. The overall core workflow and architectural schematic of the framework are summarized in Figure 1.

The core module provides foundational, platform-wide utilities and definitions, including enumeration types for tasks and models, configuration management, caching mechanisms, and error handling. The structures module offers tools for atomic structure manipulation and geometry operations, featuring specialized support for two-dimensional materials, symmetry analysis, and format conversion. The engine module handles interaction with

# UniMatSim Computational Framework Schematic

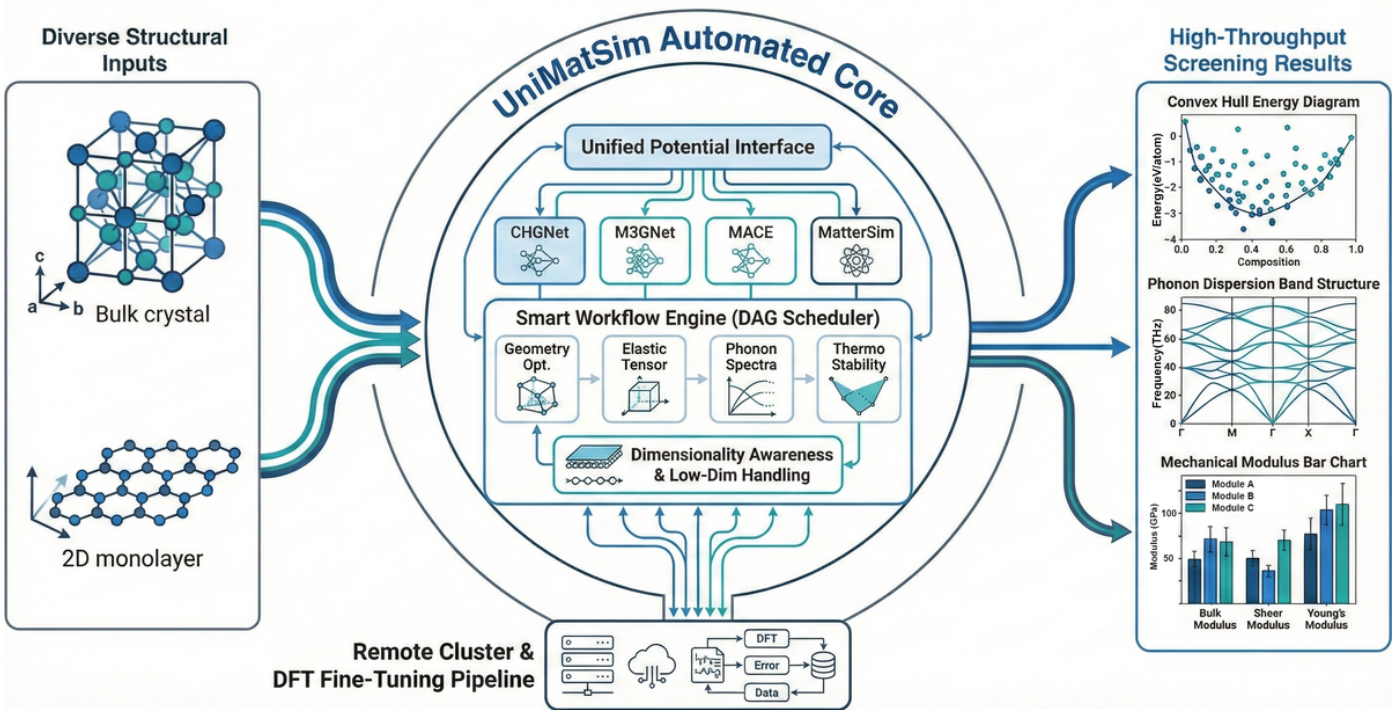


Figure 1: **Architectural overview of the UniMatSim framework.** The schematic illustrates the system’s core workflow. It accepts diverse structural inputs (e.g., bulk crystals, 2D monolayers) and processes them through the UniMatSim Automated Core. This core features a Unified Potential Interface that supports various models (CHGNet, M3GNet, MACE, MatterSim and others) and a Smart Workflow Engine (DAG Scheduler) for executing tasks such as geometry optimization, elastic tensor calculation, phonon spectra analysis, and thermodynamic stability checks. The framework integrates dimensionality awareness for low-dimensional handling and outputs high-throughput screening results, including convex hull energy diagrams, phonon dispersion band structures, and mechanical modulus bar charts.

specific computational backends ("engines" or calculators), defining the execution of calculations for a given potential model. The workflows module encapsulates higher-level workflow logic, containing classes that represent individual tasks and a WorkflowBuilder for task orchestration and dependency management. The data module manages the parsing and conversion of external DFT data; for instance, it extracts results from VASP outputs to facilitate the fine-tuning of UMLIPs. The interface module implements the user-facing APIs, comprising a programmatic Python library interface and hooks for RESTful API services. The ui module supplies the command-line interface (CLI). This modular design allows users to interact with UniMatSim flexibly: through scripted workflows using the Python API or by executing predefined workflows via the CLI.

The modular architecture enables the independent development and testing of system components. For instance, support for new potential models can be extended simply by adding corresponding calculators to the engine module, without altering workflow definitions. Similarly, new workflow tasks can be introduced without modifying the underlying computation execution. Modules interact via well-defined interfaces. A key interface is the MaterialsSimulationSystem class, accessible through the API, which acts as the primary high-level entry point by integrating core, engine, and workflow functionalities. Upon initializing a MaterialsSimulationSystem instance, the system loads default configurations, initializes caching and storage backends, and prepares the computational engines. Users can then execute workflow tasks, such as structural optimization via `system.workflow_manager.optimization(...)`. These invocations are automatically routed to the appropriate engine for computation, with results handled seamlessly. This design ensures simplicity and efficiency for common operations while offering advanced users significant customization flexibility. Examples include defining new task types by subclassing BaseTask or implementing custom storage in `core.storage`, both of which incur minimal impact on the rest of the system.

### 3. Key Technical Implementations

To translate the modular architecture described above into a robust computational platform, UniMatSim incorporates several critical technical implementations. These components are designed to resolve the fragmentation of the current ecosystem while providing a standardized, automated execution environment. In this section, we elaborate on the specific engineering strategies employed, ranging from the foundational abstraction of diverse potential models and data-driven fine-tuning workflows to the high-level orchestration of complex simulation tasks and the implementation of flexible local-remote interaction modes.

#### 3.1. Unified Machine Learning Interatomic Potential Interface

A core feature of UniMatSim is its unified interface for diverse interatomic potentials, implemented via the CalculationInvocation class for consistent potential management. Implementation-wise, UniMatSim utilizes the Atomic Simulation Environment (ASE[19]) as its primary calculator backend. For instance, selecting the Lennard-Jones potential[20] triggers the engine module to instantiate ASE's LennardJones calculator and associate it with the atomic structure. For machine learning potentials like M3GNet and CHGNet, UniMatSim either calls their native Python implementations or wraps them via ASE's external interface when available. All calculators conform to a unified interface for computing energy, forces, stress, and related properties. This abstraction allows high-level workflow tasks to be model-agnostic, insulating them from implementation specifics. This design aligns with ASE's philosophy of a unified Calculator interface, which UniMatSim generalizes and embeds within a comprehensive workflow framework. Consequently, users can switch between models seamlessly by invoking the `set_potential_model()` method, leaving downstream calculation code unchanged. The interface currently supports:

- UMLIPs: CHGNet, M3GNet, MACE, MatterSim, SevenNet, DeepMD[21]
- Classical potentials: Lennard-Jones, Buckingham[22] (used for testing and validation)

#### 3.2. Data-Driven Model Fine-Tuning Support

While universal UMLIPs demonstrate strong generalization across diverse chemical spaces, fine-tuning is often necessary to enhance their accuracy for specific material systems or extreme conditions [23, 24]. To address this, UniMatSim integrates a complete data-driven fine-tuning workflow, encompassing all steps from raw data acquisition to model training.

The framework offers efficient data extraction and conversion tools through the `unimatsim.data` module. It supports the batch extraction of physical quantities—including total energy, atomic forces, and stress—from VASP output files (OUTCAR and vasprun.xml). To ensure training data quality, the `VASPDataExtraction` module implements an energy-tolerance-based structure filtering mechanism that automatically removes redundant configurations from molecular dynamics trajectories or structural relaxation pathways. The `VASPDataConverter` then transforms the extracted data into standardized formats suitable for machine learning (e.g., JSON or Extended XYZ), applying predefined thresholds to filter outlier energies or excessively large forces.

Once data preparation is complete, the framework provides a unified command-line interface for fine-tuning

(`unimatsim model fine-tuning`), compatible with several universal potentials such as CHGNet and MatterSim. It includes comprehensive support for validation: users can specify a separate validation data file with the `--valid-material` argument or automatically reserve a fraction (default: 0.1) of the training data via `--valid-split`. An early-stopping strategy is configured with the `--early-stop-patience` argument (default: 10), which halts training if the validation loss fails to improve over consecutive epochs, thereby mitigating overfitting. For scenarios requiring detailed control, a JSON configuration file can be supplied with `--config` to define advanced hyperparameters such as force and stress loss weights (`force_loss_ratio`, `stress_loss_ratio`), energy renormalization (`re_normalize`), and learning-rate decay step size (`step_size`).

After fine-tuning, the system creates an output directory named `ft_<model>_<name>` containing the final fine-tuned model (`<model>_finetuned.pth`), the best checkpoint (`best_model.pth`), and periodically saved intermediate checkpoints. The resulting model can be referenced directly in subsequent workflow configurations.

### 3.3. Modular Task Architecture and Computational Capabilities

To ensure extensibility and maintainability, UniMatSim adopts a modular architecture that abstracts complex simulation procedures into discrete, self-contained units referred to as *Tasks*. Rather than hard-coding simulation logic, the framework utilizes a dynamic registration mechanism based on the decorator pattern. This design decouples the definition of physical protocols from the workflow execution engine, allowing for the seamless integration of novel computational methods without altering the core infrastructure.

Significantly, a *Task* in UniMatSim encapsulates more than a single atomic operation; it orchestrates comprehensive, multi-stage physical workflows. For instance, the elastic constant calculation (ELASTIC) is not merely a function call but an automated pipeline that sequentially executes structural relaxation, symmetry-adapted strain generation, energy-force evaluation, and stress-strain fitting. This high-level abstraction ensures methodological consistency and reproducibility across high-throughput screening campaigns, reducing the potential for human error in complex simulation chains.

UniMatSim currently integrates nine core task modules, categorized into four functional domains:

#### A. Structural Optimization and Symmetry Analysis

- 1. Geometry Optimization (OPTIMIZATION):** Implements robust energy minimization protocols using algorithms such as BFGS, FIRE, and LBFGS. The module allows for precise control over convergence criteria, including force thresholds and maximum iter-

ation steps, ensuring reliable ground-state structure determination.[25, 19]

- 2. Symmetry Characterization (SYMMETRY):** Integrates `spglib` to automatically identify space groups and standardized primitive cells, essential for reducing computational cost and classifying material topology.[26]
- 3. Static Calculation (SINGLE\_POINT):** Performs single-point evaluations of energy, forces, and virial stresses. This module serves as a fundamental building block for data generation and potential validation.

#### B. Mechanical and Dynamical Properties

- 1. Elastic Stiffness Tensor (ELASTIC):** Automates the calculation of second-order elastic constants via the stress-strain method. The module derives bulk, shear, and Young’s moduli while rigorously checking mechanical stability criteria.[27, 28, 29, 30, 31]
- 2. Equation of State (EOS):** Fits energy-volume data to the Birch-Murnaghan equation of state to determine equilibrium lattice parameters and bulk moduli under hydrostatic conditions.[32]
- 3. Phonon Dispersion (PHONON):** Computes phonon spectra and density of states (DOS) using the finite displacement method[33, 34]. It features automated generation of high-symmetry band paths[35] for Brillouin zone sampling.
- 4. Molecular Dynamics (MOLECULAR\_DYNAMICS):** Facilitates finite-temperature simulations under NVE ensembles, enabling the analysis of thermodynamic evolution and transport phenomena through mean squared displacement (MSD) calculations.

#### C. Thermal Transport Properties

- 1. Boltzmann Transport Solver (BTE):** Interfaces with `phono3py` to evaluate lattice thermal conductivity by solving the linearized Boltzmann transport equation, accounting for anharmonic phonon-phonon interactions.[36, 37, 38, 39]

#### D. High-Throughput Data Curation

- 1. Data Ingestion (VASP\_EXTRACT):** Provides automated parsing routines for batch extraction and standardization of physical quantities from legacy DFT outputs (e.g., VASP), facilitating the construction of training datasets for machine learning potentials.

### 3.4. Workflow Scheduling Strategy (*WorkflowBuilder*)

Task dependencies are managed by the workflow engine to enforce correct execution order and to accommodate complex workflow topologies. Each task class specifies its inputs—commonly an atomic structure and calculation parameters—and outputs, such as a relaxed structure or computed material properties. During workflow construction, a task’s output can be passed as input to downstream tasks. UniMatSim’s *WorkflowManager* (accessible via `system.workflow_manager`) works in tandem with the underlying *WorkflowBuilder* to track these dependencies. For straightforward sequential operations (e.g., a chain of `optimization()`, `elastic()`, `phonon()` calls), outputs are automatically forwarded. For more intricate patterns, the *WorkflowBuilder* allows explicit definition of dependency graphs, where users can construct directed acyclic graphs (DAGs) from task nodes and edges, mixing serial and parallel execution as needed.

The *WorkflowBuilder* further provides flexible topology and parallel-synchronization control. Users can define join tasks that wait for several predecessor branches to finish. For instance, after a structure relaxation (`relax`), both elastic constant (`elastic`) and phonon spectrum (`phonon`) calculations can be launched in parallel; a final stability evaluation (`stability`) is then triggered only after both complete. This branch-and-join logic can be expressed concisely as a Python dictionary: `"relax": ["elastic", "phonon"], "elastic": "stability", "phonon": "stability", "stability": None`. The *WorkflowBuilder* automatically schedules the execution: first `relax`, then concurrent `elastic` and `phonon` tasks, and finally `stability` once the parallel branches succeed. This abstracts away all low-level concurrency and synchronization details, requiring no manual threading or scheduling code from the user.

Additionally, the framework implements a checkpointing mechanism that periodically persists intermediate results to disk or a database, linking them to a unique workflow hash ID. If a task fails or the run is interrupted, the workflow can resume from the last valid checkpoint, avoiding a full restart. This feature is especially valuable for lengthy or computationally unstable simulations.

### 3.5. API and Remote Invocation

UniMatSim’s programmatic interface supports the complete development cycle, from interactive scripting to fully automated pipeline deployment. Its core Python API centers on the `MaterialsSimulationSystem` class. This class integrates essential operations—including model configuration, structure loading, engine management, and workflow orchestration—into a single, coherent entry point. The design ensures seamless interoperability with established structure representation libraries such as `Pymatgen` and `ASE`, accepting `Structure` or `Atoms` objects directly and returning results as standardized Python dictionaries or objects containing energy, forces, stress, and associated metadata.

To facilitate access to distributed computational resources, UniMatSim implements remote model invocation within its `engine` module. This is especially valuable for machine-learning potentials that require specialized hardware (e.g., GPUs) or specific software environments. The `ModelInvocation` class allows users to toggle between two operational modes: `DIRECT` (local execution) and `REMOTE`. In remote mode, the `RemoteCalculator` packages the atomic structure and calculation parameters, transmitting them via a REST API (built with `FastAPI`[40, 41]) to a remote server. The invocation remains transparent to the user, and results are returned in the same unified format as local calls, guaranteeing processing consistency.

The command-line interface (CLI) mirrors this dual-mode capability, governed by an `InvocationMode` enumeration. Remote execution is activated with the `--remote` flag, with server location specified by `--host` and `--port`; authentication can be supplied via `--api-key`. For instance:

```
# Local-mode elastic constant calculation
unimatsim calc elastic -i Si.cif -m mattersim

# Remote-mode execution
unimatsim calc elastic -i Si.cif -m chgnet --remote
--host 192.168.1.100 --port 8000
```

This unified dual-mode architecture offers distinct benefits for distributed computing. Users can design and manage workflows on modest local workstations while offloading compute-intensive steps—such as single-point energy evaluations for elastic or phonon calculations—to remote clusters equipped with GPUs or high-performance CPUs. The local machine then only handles lightweight orchestration and result aggregation, eliminating the need to deploy full software stacks and large model files on every node. Moreover, the architecture promotes collaborative research: multiple groups can share a centralized computing service, reducing the overhead of maintaining disparate software environments and enhancing both resource efficiency and reproducibility across studies.

### 3.6. Command-Line Interface and Interaction Design

To facilitate seamless integration into high-performance computing (HPC) environments and automated pipelines, UniMatSim provides a robust Command-Line Interface (CLI) constructed upon the `Typer` framework [41, 42]. The CLI is structured around a modular hierarchy, compartmentalizing functionality into four distinct domains: property evaluation (`calc`), workflow orchestration (`workflow`), data ingestion (`data`), and post-processing analysis (`analysis`).

#### 3.6.1. Direct Property Evaluation Module

The `calc` module orchestrates the execution of fundamental physical property solvers. It serves as the primary entry point for launching atomic simulations, supporting

both single-task execution and batch parallelization. Key capabilities include:

- 1. Geometry Optimization:** The system enables rapid ground-state determination. For instance, `unimatsim calc optimize -i Si.cif -m chgnet` performs relaxation on a single structure. To maximize resource utilization on multi-core nodes, batch processing can be invoked via `unimatsim calc optimize -i ./structures/ -m mattersim --parallel 4`, which distributes optimization tasks across four concurrent processes.
- 2. Elastic Stiffness Tensor:** The command `unimatsim calc elastic -i optimized.cif -m mattersim` automates the deformation-energy method to derive the elastic tensor. Crucially, the `--check-stability` flag integrates an on-the-fly evaluation of the Born-Huang mechanical stability criteria, filtering unstable candidates immediately after computation.
- 3. Phonon Dispersion:** Vibrational properties are computed using the finite displacement method. The command `unimatsim calc phonon -i structure.cif --supercell 2 2 2 --mesh 10 10 10 -m chgnet` specifies the supercell expansion matrix via `--supercell` and the Brillouin zone sampling density via `--mesh`, automating the generation of force constants and band structures.
- 4. Molecular Dynamics:** Finite-temperature evolution is simulated using commands such as `unimatsim calc md -i initial.cif --ensemble nvt --temperature 300 --steps 10000 -m m3gnet`. This module supports standard ensembles (NVE, NVT, NPT) and provides granular control over thermodynamic parameters, enabling the study of phase stability and diffusion kinetics.

### 3.6.2. Automated Workflow Orchestration Module

The `workflow` module manages complex simulation pipelines by defining tasks as nodes in a Directed Acyclic Graph (DAG). This approach handles dependency resolution and concurrent execution via declarative configuration files (YAML/JSON).

- 1. Declarative Configuration Generation:** Users can rapidly scaffold complex pipelines using the generator command. For example, `unimatsim workflow create -o workflow.yaml -s opt,elastic,phonon -m mattersim` synthesizes a complete configuration file for a sequential relaxation-elastic-phonon workflow. The resulting YAML artifact (shown below) encapsulates all execution parameters and dependency logic:

```

1 metadata:
2   description: "Sequential workflow generated from:
3     opt, elastic, phonon"
4   ml_potential: "mattersim"
5   ml_params:

```

```

5     model_path: "best_model.pth"
6     potential_type: "ml"
7
8 tasks:
9   - name: "optimization"
10    type: "optimize"
11    config:
12      fmax: 0.01
13      steps: 500
14      optimizer: "BFGS"
15
16   - name: "elastic"
17    type: "elastic"
18    config:
19      fmax: 0.1
20      relax_structure: true
21      check_stability: true
22      norm_strains: [-0.01, -0.005, 0.005, 0.01]
23      shear_strains: [-0.06, -0.03, 0.03, 0.06]
24
25   - name: "phonon"
26    type: "phonon"
27    config:
28      supercell: [2, 2, 2]
29      mesh: [10, 10, 10]
30      check_stability: true
31      save_bandstructure: true
32
33 dependencies:
34   optimization: "elastic"
35   elastic: "phonon"
36   phonon: null

```

- 2. Workflow Execution and Scheduling:** The command `unimatsim workflow run -C workflow.yaml -i ./structures/` initiates the workflow engine. The system topologically sorts the task graph and executes independent nodes in parallel where possible. State persistence is handled automatically, generating a `.checkpoint_<workflow_id>.json` log to track task completion.
- 3. Fault Tolerance and Recovery:** To mitigate interruptions in long-running simulations, the framework supports state recovery via `unimatsim workflow resume --id <workflow_id> -C workflow.json`. This mechanism ensures that calculations can be resumed from the last successful checkpoint, significantly improving efficiency in unstable computational environments.

### 3.6.3. Data Ingestion and Transformation Module

The `data` module functions as an ETL (Extract, Transform, Load) pipeline, bridging the gap between first-principles raw data and machine learning training requirements.

- 1. High-Throughput Extraction:** The command `unimatsim data import vasp -i ./vasp_results/ -o extracted_data.json` parses large directories of VASP outputs, extracting key physical quantities (energy, forces, stress tensors). The `--converged-only` filter ensures data quality by discarding unconverged calculation results.

- 2. Structure Serialization:** For bulk structure processing, `unimatsim data import poscar -i ./POSCAR_files/ -o structures.csv --format csv` aggregates lattice parameters and atomic coordinates from multiple POSCAR files into a tabular format suitable for statistical analysis.
- 3. Training Data Standardization:** To facilitate model training, `unimatsim data convert to-xyz -i ./structures/ -o ./training_data/` converts structural datasets into the Extended XYZ format, a standard input format for many modern machine learning potential frameworks.
- 4. Dataset Partitioning:** Large datasets can be managed using `unimatsim data slide -i large_dataset.json -o chunks/ --chunk-size 1000`, which segments data into manageable shards based on record count, optimizing memory usage during subsequent training or analysis steps.

#### 3.6.4. Post-Processing and Validation Module

The `analysis` module provides tools for structural characterization and the comparative validation of model predictions.

- 1. Symmetry Identification:** The command `unimatsim analysis symmetry -i optimized_structures/ --symprec 0.01` employs `spglib` to determine crystal systems, space groups, and point groups. The `--symprec` parameter allows for tunable numerical tolerance, while `--filter` enables the selective screening of structures based on symmetry constraints.
- 2. Consensus Stability Analysis:** `unimatsim analysis compare module -i ./results/ -o stability_comparison.png` facilitates multi-model cross-validation. It automatically generates UpSet plots[43] to visualize the intersection of stability predictions (e.g., formation energy, phonon stability) across different potentials, aiding in the identification of high-confidence candidates through model consensus.

#### 3.7. Low-Dimensional Material Identification and Stability Analysis Strategy

Low-dimensional materials, particularly two-dimensional (2D) systems, exhibit distinct physical properties compared to their three-dimensional counterparts, necessitating specialized handling in structural identification, simulation setup, and analysis. To this end, UniMatSim incorporates a dedicated 2D material support framework within its `structures/materials_2d` module. This framework leverages `pymatgen`'s[44] dimensionality analysis tools to automatically assess the dimensionality of an input crystal structure. The algorithm analyzes the

atomic connectivity matrix and periodic boundary conditions, employing graph-theoretic methods to determine the spatial connectivity of the bonding network. A structure is classified as 2D if it exhibits continuous in-plane covalent bonding with significant van der Waals gaps in the perpendicular direction. This approach provides more accurate identification of genuine layered materials compared to simple heuristics based on lattice parameter ratios, and can also recognize other low-dimensional forms such as one-dimensional nanotubes and zero-dimensional clusters.

Based on this identification, UniMatSim automatically tailors subsequent simulation steps. For instance, during structural relaxation, the `apply_2d_cell_filter()` function constrains the unit cell using ASE's `FrechetCellFilter`[25, 19] with a default `mask=[1,1,0,0,0,1]`, permitting only in-plane lattice and atomic relaxation to preserve physically meaningful interlayer distances. For phonon and Boltzmann transport equation (BTE) calculations, supercell construction is adjusted from  $(n,n,n)$  to  $(n,n,1)$  to eliminate unnecessary computational cost along the non-periodic direction. Furthermore, the `get_filtered_2d_bz_path()` function generates an appropriate Brillouin zone path by excluding high-symmetry points with a non-zero  $k_z$  component, thereby preventing artifacts from spurious out-of-plane dispersion. These automated protocols minimize manual input and enhance the reliability and consistency of simulations for low-dimensional materials.

Stability assessment is crucial for identifying synthesizable candidates in high-throughput screening. UniMatSim evaluates stability from three complementary perspectives: elastic, dynamic, and thermodynamic. Elastic stability is verified by the `stability_test_3d()` and `stability_test_2d()` functions, which check the positive definiteness of the elastic tensor according to the Born–Huang criteria. The implementation supports the stability conditions for all seven crystal systems (cubic, hexagonal, tetragonal, orthorhombic, monoclinic, triclinic, and rhombohedral[45]) and includes specific 2D criteria for common 2D lattice types (e.g., hexagonal, square, rectangular). Dynamic stability is analyzed by the `PhononStabilityChecker` module, which scans the phonon spectrum for soft modes or imaginary frequencies. Different thresholds are applied to high-symmetry points and general  $k$ -points (default:  $-0.005$  eV and  $-0.001$  eV, respectively) to distinguish genuine instabilities from numerical noise. Thermodynamic stability is assessed by the `ThermalStabilityChecker`, which calculates the formation energy and the energy above the convex hull[46] to gauge a material's phase stability. This process can interface with the Materials Project API[47] to automatically fetch data on competing phases for comparison.

## 4. Application Example

### 4.1. High-Throughput Lieb-Lattice Screening Workflow

To demonstrate the performance of UniMatSim in complex material discovery, we applied it to high-throughput stability screening of two-dimensional Lieb lattices and their derivatives—systems notable for their unique structural and electronic properties. The Lieb lattice is a canonical model for studying strong electron correlations[48]. Its unit cell comprises three inequivalent atomic sites and hosts characteristic flat electronic bands[49], making it a valuable platform for investigating magnetic, superconducting[50], and topological phenomena[51]. These features, however, also demand high accuracy and efficiency from computational methods.

We implemented a systematic screening workflow, illustrated in figure 2, using a machine-learning potential previously optimized for 2D materials[52]. The workflow follows a coarse-to-fine, condition-triggered strategy: progressively applying stricter stability filters (elastic, dynamic, thermodynamic) only to candidates that pass earlier, less expensive stages. This approach maximizes computational efficiency while maintaining physical rigor.

The initial candidate set contained 1,176 distinct Lieb lattice compositions spanning 36 chemical elements—a diverse chemical space. These included 29 transition metals (Ag, Au, Cd, Co, Cr, Cu, Fe, Hf, Hg, Ir, Mn, Mo, Nb, Ni, Os, Pd, Pt, Re, Rh, Ru, Sc, Ta, Tc, Ti, V, W, Y, Zn, Zr), 4 chalcogens (O, S, Se, Te), and 3 pnictogens (As, N, P). In the prototypical structure (Figure 4a), two symmetry-inequivalent transition-metal sites occupy the (0, 0.5, 0.5) and (0.5, 0, 0.5) positions, a third transition-metal site resides at (0, 0, 0.5), and the four equivalent ligand sites are filled by either chalcogen or pnictogen atoms.

To efficiently filter out unstable structures prior to computationally expensive high-precision DFT calculations, this study employs a rapid pre-screening workflow based on the MatterSim machine-learning potential to conduct a multi-dimensional stability assessment of the initial candidates, as illustrated in Figure 2.

*Step 1: Structural optimization and preprocessing.* All initial candidates were first subjected to rigorous geometry optimization using the MatterSim machine-learning potential for energy and force evaluation and the BFGS algorithm for ionic relaxation. Convergence was achieved when the maximum residual force component fell below  $f_{\max} \leq 0.05$  eV/Å, a threshold chosen to balance accuracy and computational cost. Given the 2D nature of the Lieb lattice, the framework automatically engaged its specialized 2D optimization routine, applying in-plane relaxation constraints via the FrechetCellFilter (mask = [1, 1, 0, 0, 0, 1]) to prevent unphysical changes in the interlayer distance. The resulting relaxed structures served as the baseline for all subsequent property evaluations.

*Step 2: High-throughput elastic stability screening.* The second-order elastic stiffness tensor  $C_{ij}$  was computed for each optimized structure. Because Lieb lattices typically exhibit square or rectangular symmetry, the corresponding Born-Huang criteria were applied automatically: for a square lattice,  $C_{11} > |C_{12}|$  and  $C_{66} > 0$ ; for a rectangular lattice,  $C_{11} > 0$ ,  $C_{22} > 0$ ,  $C_{66} > 0$ , and  $C_{11}C_{22} - C_{12}^2 > 0$ . This screening was performed using the finite displacement method, which is computationally much cheaper than a full phonon calculation and thus efficiently filters out mechanically unstable ("soft") candidates.

*Step 3: Selective phonon calculations.* Only structures that passed the elastic stability test proceeded to full phonon spectrum calculations. An appropriate supercell (typically  $5 \times 5 \times 1$ , avoiding spurious interactions along the non-periodic direction) was constructed automatically. The dynamical matrix was computed via the finite displacement method and diagonalized along the high-symmetry path  $\Gamma$ -X-M- $\Gamma$  to obtain the phonon dispersion. The primary indicator of dynamic instability was the presence of imaginary frequencies ( $\omega^2 < 0$ ), which can occur even in elastically stable materials due to complex vibrational modes.

*Step 4: Integrated stability assessment and classification.* The results from steps 1-3 were combined to assign a multi-dimensional stability rating to each candidate: (1) Fully stable (passes both elastic and dynamic tests); (2) Elastically unstable (fails the Born-Huang criteria); (3) Dynamically unstable (elastically stable but exhibits imaginary phonon frequencies). The workflow finally produced a structured report containing key properties such as formation energy, elastic constants, and the location and magnitude of any imaginary frequencies.

To further enhance result reliability, we fine-tuned the MatterSim potential, generating four independent model variants trained with different random seeds (42, 123, 2025, 8888; see SI for details), as shown in Figure 2. Multi-model cross-validation identified 393 stable structures.

To quantify workflow efficiency, all calculations were executed on a high-performance computing cluster with AMD EPYC 9354 processors (192 cores per node). Batch runs used 2 nodes (64 CPU cores in total) for parallel processing. With the MatterSim-2D potential [52], the average processing time per structure was 4.6 s, distributed as follows: structural optimization  $\sim 0.5$  s, elastic-constant calculation  $\sim 0.4$  s, and phonon calculation  $\sim 3.8$  s. This cost is substantially lower than that of DFT, demonstrating the efficiency and robustness of UniMatSim for the automated screening of complex low-dimensional materials. The framework's conditional execution and dedicated 2D material support thus provide a reliable platform for large-scale exploration of novel quantum materials. The high-throughput DFT screening workflow is illustrated in Figure 3. Starting with the 393 structures that passed the

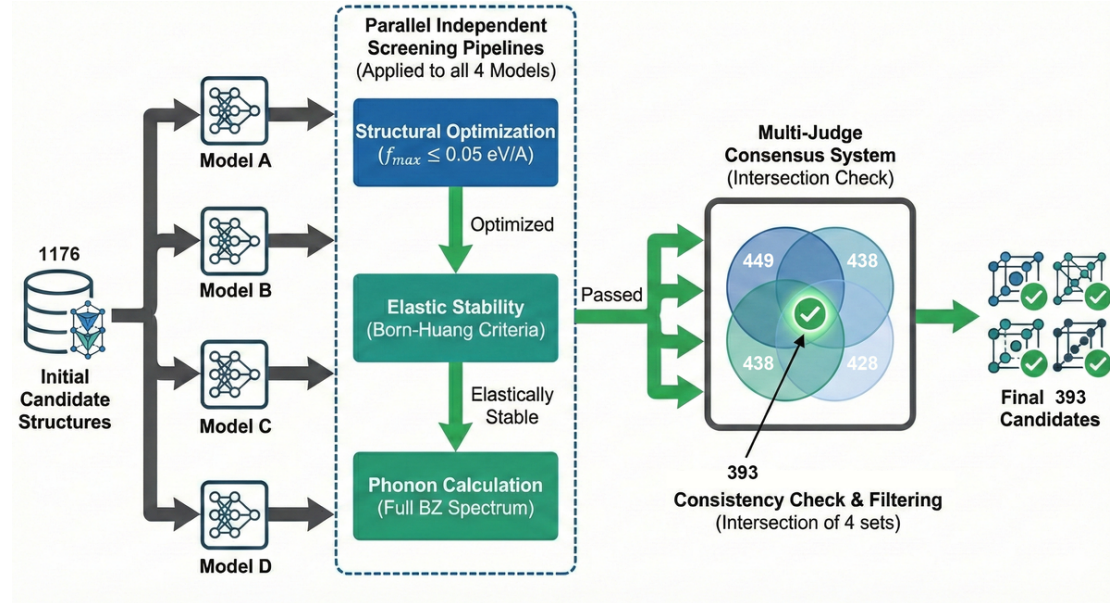


Figure 2: **High-throughput stability-screening workflow for Lieb lattices implemented in UniMatSim.** The diagram illustrates the parallel screening process starting from 1176 initial candidate structures. Four independent models (Models A–D) are employed to run parallel screening pipelines, each performing structural optimization (convergence criteria  $f_{max} \leq 0.05$  eV/Å), elastic stability verification, and phonon spectrum calculations. The individual models identified 449, 438, 438, and 428 stable candidates, respectively. These sets enter the Multi-Judge Consensus System, where a strict intersection check confirms 393 final consistent candidates for subsequent analysis.

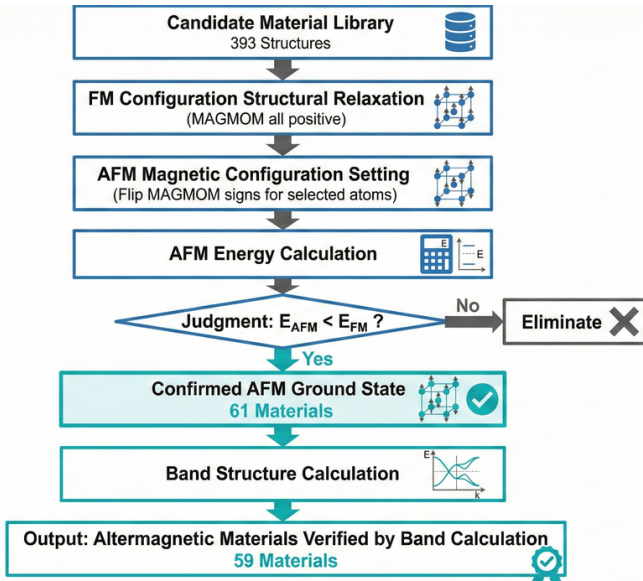


Figure 3: Workflow for the identification of altermagnetic Lieb lattices. The process begins with the relaxation of 393 candidates in a ferromagnetic (FM) state. Antiferromagnetic (AFM) configurations are generated by flipping the spin signs (MAGMOM) of specific atoms. Candidates are retained only if the AFM state is energetically more favorable than the FM state ( $E_{AFM} < E_{FM}$ ). The resulting 61 AFM-stable structures undergo band structure analysis to verify altermagnetism, yielding 59 final candidates.

preliminary stability screening, we evaluated their magnetic ground states by comparing the total energies of ferromagnetic (FM) and antiferromagnetic (AFM) configurations. The AFM states were constructed by flipping specific atomic spins within the relaxed FM structures. Only systems satisfying the energetic criterion  $E_{AFM} < E_{FM}$ —indicating a stable AFM ground state—were retained. This magnetic screening narrowed the candidate pool to 61 structures, which subsequently underwent DFT band-structure calculations (computational details provided in the Supplementary Information). Ultimately, 59 Lieb-lattice candidates exhibiting staggered-magnetic-band characteristics were selected; their fundamental data are compiled in the SI.

Among these 59 final candidates, the chemical diversity was reduced from the initial 36 to 26 element types (72.2% retention). Transition metals decreased from 29 to 22, chalcogens from 4 to 3 (oxygen was eliminated), and pnictogens to phosphorus alone (N and As were excluded). Manganese emerged as the most frequent element, appearing in 30 of the 59 materials (50.8%), underscoring the pivotal role of  $Mn^{2+}$  (high-spin  $d^5$ ) in stabilizing the magnetic Lieb lattice, followed by Fe (37.3%) and Co (11.9%). Among the ligands, selenium (39.0%) surpassed sulfur (30.5%) as the dominant chalcogen, with tellurium (28.8%) also well represented. Phosphorus (P) was retained but appears only in the single compound  $Fe_2TcP_4$ . The strong presence of 4d/5d heavy transition metals (Tc, Mo, Os, Re, Ru, W) highlights their utility in tuning magnetic exchange and spin-orbit coupling.

We discuss  $TaCo_2Se_4$  as a representative structure. It

exhibits the prototypical Lieb-lattice geometry: Co atoms occupy the (0, 0.5, 0.5) and (0.5, 0, 0.5) sites, Ta resides at (0, 0, 0.5), and Se atoms populate the four equivalent ligand positions. As shown in Figure 4(b), the front and top views clearly reveal the metal-atom skeleton and its characteristic symmetry. The calculated band structure (Figure 4c) exhibits clear spin splitting, a direct signature of the staggered-magnetic-band character. (Band structures for the remaining 58 candidates are provided in the Supplementary Information.)

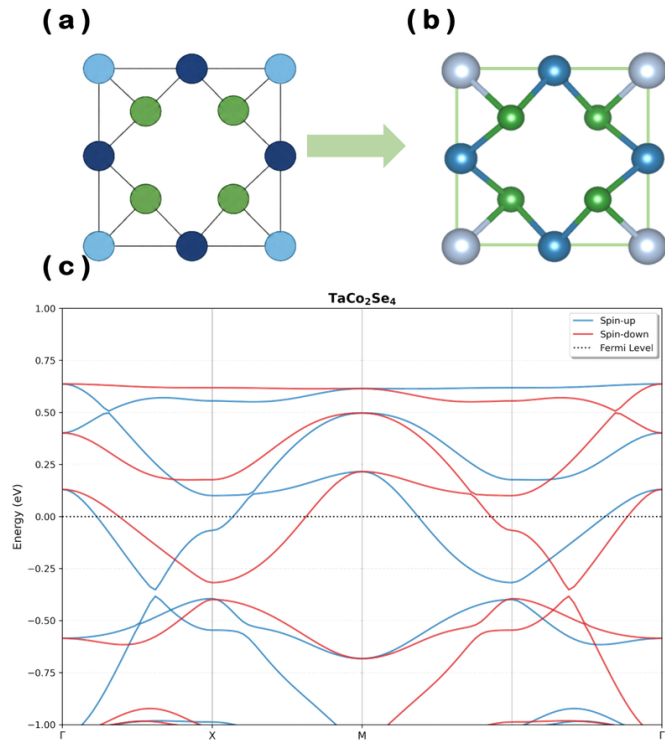


Figure 4: Geometry and electronic structure of the representative Lieb-lattice material TaCo<sub>2</sub>Se<sub>4</sub>. (a) Schematic of the Lieb lattice: light blue and dark blue spheres denote two distinct transition-metal sites, and green spheres denote chalcogen or pnictogen sites. (b) Atomic structure of TaCo<sub>2</sub>Se<sub>4</sub> showing the Lieb-lattice framework and coordination environment. Co, Ta, and Se atoms are colored dark blue, light blue, and green, respectively. (c) DFT-calculated spin-polarized band structure, revealing the characteristic spin splitting and staggered-magnetic-band character.

## 5. Discussion

### 5.1. Comparison with Existing Tools

UniMatSim is designed specifically for high-throughput screening with UMLIPs. Unlike frameworks such as ASR and Atomate, which are built primarily around DFT, UniMatSim natively incorporates mainstream UMLIPs (e.g., CHGNet, M3GNet, MatterSim) at the architectural level. A unified `set_potential_model()` interface allows seamless switching between potentials, enabling the same workflow to be applied across different models without modification. Coupled with its remote-invocation capability,

the framework can transparently offload calculations to high-performance servers, offering substantial scalability for resource-constrained environments.

Regarding deployment complexity, UniMatSim adopts a lightweight strategy, contrasting with the heavier requirements of tools like Atomate and AiiDA. Atomate requires a MongoDB database and the FireWorks scheduler; AiiDA depends on PostgreSQL and a complex plugin ecosystem. Such dependencies can be prohibitive for small- to medium-scale screenings. In contrast, UniMatSim stores results directly as JSON files [53] on the filesystem. Users need only a standard Python environment with ASE and pymatgen to run calculations locally or on an HPC cluster. The FastAPI-based remote mode further enables "zero-deployment" operation: all potential evaluations are performed on a remote server, so no model files or specialized backends need be installed locally.

Usability is enhanced by dual interfaces—a Python API and a command-line tool. The CLI's `workflow create --sequence` command, for instance, generates complete workflow configurations from simple strings (e.g., `opt, elastic, phonon`). Remote execution is seamlessly integrated: adding flags like `--remote` and `--host` redirects the workflow to a remote cluster, maintaining a consistent user experience.

A key strength is the integrated, tripartite stability assessment. The framework combines (i) elastic stability tests (Born–Huang criteria for all crystal systems), (ii) dynamic stability checks (phonon imaginary-frequency analysis), and (iii) thermodynamic stability evaluation (convex-hull analysis via the Materials Project API). This unified pipeline eliminates the need to cobble together separate tools for end-to-end screening.

Finally, UniMatSim offers built-in support for low-dimensional materials. Using pymatgen's dimensionality detection, it automatically identifies 2D systems and adjusts simulation parameters accordingly: phonon supercells are set to  $(n, n, 1)$ , structural relaxation is constrained to the plane via `FrechetCellFilter`, and Brillouin-zone paths exclude out-of-plane high-symmetry points. In general-purpose frameworks (e.g., Atomate, AiiDA), achieving the same adaptations requires extensive manual configuration. UniMatSim automates these steps through functions like `detect_2d_material()`, boosting both reliability and efficiency for low-dimensional material discovery.

### 5.2. Future Development Directions

Future development of UniMatSim will focus on: (1) expanding support for emerging UMLIPs; (2) implementing an active-learning workflow to close the loop between ML potential evaluation, DFT validation, and model refinement; (3) developing a Textual-based terminal user interface (TUI) to improve accessibility for non-programmers; (4) integrating database backends (e.g., MongoDB) for enhanced management of large-scale simulation data.

## 6. Conclusion and Outlook

We have presented UniMatSim, a comprehensive Python framework for high-throughput materials simulation. The framework integrates a unified interface for machine-learning potentials, a modular task-registration system, dedicated support for two-dimensional materials, and a robust multi-faceted stability-verification workflow. Together, these features offer an efficient and reliable platform for computational materials research. Our validation demonstrates that UMLIP-based calculations achieve accuracy comparable to DFT while offering speedups of 2–3 orders of magnitude, thus providing a powerful foundation for large-scale materials screening and discovery.

## Acknowledgements

UniMatSim builds upon several key open-source projects, including pymatgen for materials analysis, ASE for atomistic simulations, phono3py for phonon calculations, and the original implementations of machine-learning interatomic potentials such as CHGNet, M3GNet, and MACE. While our framework was developed independently, we acknowledge the `matcalc` package for its early work in this area, which provided valuable inspiration for our own methodological objectives. We also extend our sincere gratitude to Dr. Jielan Li of Microsoft for their valuable contributions to the Boltzmann Transport Equation (BTE) code. This work was supported by the Open Research Fund of State Key Laboratory of Precision and Intelligent Chemistry and the National Natural Science Foundation of China (Grant No. 22203026). During the preparation of this manuscript, the authors used GPT-5 to improve text readability and coherence and Claude 4.5 to assist with code optimization.

## References

- [1] L. Himanen, A. Geurts, A. S. Foster, P. Rinke, Data-driven materials science: Status, challenges, and perspectives, *Adv. Sci.* 7 (2) (2020) 1903667.
- [2] D. Sivan, K. S. Kumar, A. Abdullah, V. Raj, I. I. Misnon, S. Ramakrishna, R. Jose, Advances in materials informatics: A review, *J. Mater. Sci.* 59 (10) (2024) 2602–2643.
- [3] H. Daglar, S. Keskin, Recent advances, opportunities, and challenges in high-throughput computational screening of MOFs for gas separations, *Coord. Chem. Rev.* 422 (2020) 213470.
- [4] H. M. Polat, S. Kavak, H. Kulak, A. Uzun, S. Keskin, CO<sub>2</sub> separation from flue gas mixture using [BMIM][BF<sub>4</sub>]/MOF composites: Linking high-throughput computational screening with experiments, *Chem. Eng. J.* 394 (2020) 124916.
- [5] J. E. Fowler, M. A. Kottwitz, N. Trask, R. Dingreville, Beyond combinatorial materials science: The 100 prisoners problem, *Integr. Mater. Manuf. Innov.* 13 (1) (2024) 83–91.
- [6] K. S. Jakob, A. Walsh, K. Reuter, J. T. Margraf, Learning crystallographic disorder: Bridging prediction and experiment in materials discovery, *Adv. Mater.* (2025) e2405148.
- [7] A. S. Palakkal, Y. Yue, S. A. Mohamed, J. Jiang, Exploiting metal-organic frameworks for vinylidene fluoride adsorption: From force field development, computational screening to machine learning, *Environ. Sci. Technol.* 58 (37) (2024) 16465–16474.
- [8] S. Jain, R. Jain, K. R. Rao, A. Bhowmik, Leveraging machine learning to minimize experimental trials and predict hot deformation behaviour in dual phase high entropy alloys, *Mater. Today Commun.* 41 (2024) 110813.
- [9] H. C. Ozdemir, A. Nazarahari, B. Yilmaz, D. Canadinc, E. Bedir, R. Yilmaz, U. Unal, H. J. Maier, Machine learning-informed development of high entropy alloys with enhanced corrosion resistance, *Electrochim. Acta* 476 (2024) 143722.
- [10] S. Batzner, A. Musaelian, L. Sun, M. Geiger, J. P. Mailoa, M. Kornbluth, N. Molinari, T. E. Smidt, B. Kozinsky, E(3)-equivariant graph neural networks for data-efficient and accurate interatomic potentials, *Nat. Commun.* 13 (2022) 2453.
- [11] D. Bidoggia, N. Manko, M. Peressi, A. Marrazzo, AiiDA-TrainsPot: Towards automated training of neural-network interatomic potentials, *Mater. Cloud Arch.* (Jan. 2026).
- [12] B. Deng, P. Zhong, K. Jun, J. Riebesell, K. Han, C. J. Bartel, G. Ceder, CHGNet as a pretrained universal neural network potential for charge-informed atomistic modelling, *Nat. Mach. Intell.* 5 (2023) 1031–1041.
- [13] C. Chen, S. P. Ong, A universal graph deep learning interatomic potential for the periodic table, *Nat. Comput. Sci.* 2 (11) (2022) 718–728.
- [14] I. Batatia, D. P. Kovacs, G. Simm, C. Ortner, G. Csanyi, MACE: Higher order equivariant message passing neural networks for fast and accurate force fields, in: *Adv. Neural Inf. Process. Syst.*, Vol. 35, Curran Associates, Inc., 2022, pp. 11423–11436.
- [15] H. Yang, C. Hu, Y. Zhou, X. Liu, Y. Shi, J. Li, G. Li, Z. Chen, S. Chen, C. Zeni, M. Horton, R. Pinsler, A. Fowler, D. Zügner, T. Xie, J. Smith, L. Sun, Q. Wang, L. Kong, C. Liu, H. Hao, Z. Lu, MatterSim: A deep learning atomistic model across elements, temperatures and pressures (2024). [arXiv:2405.04967](https://arxiv.org/abs/2405.04967).

- [16] Y. Park, J. Kim, S. Hwang, S. Han, Scalable parallel algorithm for graph neural network interatomic potentials in molecular dynamics simulations, *J. Chem. Theory Comput.* 20 (11) (2024) 4857–4868.
- [17] A. M. Ganose, et al., Atomate2: Modular workflows for materials science, *Digit. Discov.* 4 (7) (2025) 1944–1973.
- [18] S. P. Huber, Automated reproducible workflows and data provenance with AiiDA, *Nat. Rev. Phys.* 4 (2022) 431.
- [19] A. H. Larsen, et al., The atomic simulation environment—a Python library for working with atoms, *J. Phys.: Condens. Matter* 29 (27) (2017) 273002.
- [20] J. E. Lennard-Jones, On the determination of molecular fields, *Proc. R. Soc. A* 106 (738) (1924) 463–477.
- [21] J. Zeng, et al., DeePMD-kit v3: A multiple-backend framework for machine learning potentials, *J. Chem. Theory Comput.* 21 (9) (2025) 4375–4385.
- [22] R. A. Buckingham, The classical equation of state of gaseous helium, neon and argon, *Proc. R. Soc. A* 168 (933) (1938) 264–283.
- [23] X. Liu, S. Lysgaard, J. Schiøtz, T. Vegge, Fine-tuning universal machine-learned interatomic potentials: A tutorial on methods and applications (2025). [arXiv: 2506.21935](https://arxiv.org/abs/2506.21935).
- [24] L. Zhang, H. Wang, W. E, An efficient forgetting-aware fine-tuning framework for pretrained universal machine-learning interatomic potentials, *npj Comput. Mater.* 11 (2025) 9.
- [25] E. Bitzek, P. Koskinen, F. Gähler, M. Moseler, P. Gumbsch, Structural relaxation made simple, *Phys. Rev. Lett.* 97 (17) (2006) 170201.
- [26] A. Togo, K. Shinohara, I. Tanaka, Spglib: A software library for crystal symmetry search, *Sci. Technol. Adv. Mater. Methods* 4 (1) (2024) 2384822.
- [27] O. H. Nielsen, R. M. Martin, Quantum-mechanical theory of stress and force, *Phys. Rev. B* 32 (6) (1985) 3780.
- [28] Y. Le Page, P. Saxe, Symmetry-general least-squares extraction of elastic data for strained materials from ab initio calculations of stress, *Phys. Rev. B* 65 (10) (2002) 104104.
- [29] M. Born, K. Huang, *Dynamical Theory of Crystal Lattices*, Oxford University Press, Oxford, 1954.
- [30] F. Mouhat, F.-X. Coudert, Necessary and sufficient elastic stability conditions in various crystal systems, *Phys. Rev. B* 90 (22) (2014) 224104.
- [31] Q. Wei, X. Peng, Superior mechanical flexibility of phosphorene and few-layer black phosphorus, *Appl. Phys. Lett.* 104 (25) (2014) 251915.
- [32] F. Birch, Finite elastic strain of cubic crystals, *Phys. Rev.* 71 (11) (1947) 809–824.
- [33] A. Togo, I. Tanaka, First principles phonon calculations in materials science, *Scr. Mater.* 108 (2015) 1–5.
- [34] K. Parlinski, Z. Q. Li, Y. Kawazoe, First-principles determination of the soft mode in cubic ZrO<sub>2</sub>, *Phys. Rev. Lett.* 78 (21) (1997) 4063.
- [35] Y. Hinuma, G. Pizzi, Y. Kumagai, F. Oba, I. Tanaka, Band structure diagram paths based on crystallography, *Comput. Mater. Sci.* 128 (2017) 140–184.
- [36] A. Togo, L. Chaput, T. Tadano, I. Tanaka, Implementation strategies in phonopy and phono3py, *J. Phys.: Condens. Matter* 35 (2023) 353001.
- [37] A. Togo, L. Chaput, I. Tanaka, Distributions of phonon lifetimes in Brillouin zones, *Phys. Rev. B* 91 (9) (2015) 094306.
- [38] L. Chaput, Direct solution to the linearized phonon Boltzmann equation, *Phys. Rev. Lett.* 110 (26) (2013) 265506.
- [39] J. M. Ziman, *Electrons and Phonons: The Theory of Transport Phenomena in Solids*, Oxford University Press, Oxford, 2001.
- [40] S. Ramírez, FastAPI: Modern, fast web framework for building APIs with Python 3.7+, Tech. rep., FastAPI (2024).
- [41] P. K. Narayanan, *Engineering machine learning and data REST APIs using FastAPI*, Apress, 2024, pp. 191–210.
- [42] S. Ramírez, Typer, cLI library based on Python type hints (2019).
- [43] A. Lex, N. Gehlenborg, H. Strobel, R. Vuillemot, H. Pfister, UpSet: Visualization of intersecting sets, *IEEE Trans. Vis. Comput. Graph.* 20 (12) (2014) 1983–1992.
- [44] S. P. Ong, W. D. Richards, A. Jain, G. Hautier, M. Kocher, S. Cholia, D. Gunter, V. L. Chevrier, K. A. Persson, G. Ceder, Python materials genomics (pymatgen): A robust, open-source python library for materials analysis, *Comput. Mater. Sci.* 68 (2013) 314–319.
- [45] H. Wang, T. Li, X. Liu, W. Zhu, Z. Chen, Z. Li, J. Yang, mech2d: Anefficient tool for high-throughput calculation of mechanical properties for two-dimensional materials, *Molecules* 28 (11) (2023) 4337.

- [46] C. J. Bartel, A. Trewartha, Q. Wang, A. M. Holder, G. Ceder, Physical descriptor for the Gibbs energy of inorganic crystalline solids and temperature-dependent materials chemistry, *Nat. Commun.* 10 (2019) 4168.
- [47] A. Jain, et al., Commentary: The Materials Project: A materials genome approach to accelerating materials innovation, *APL Mater.* 1 (1) (2013) 011002.
- [48] E. H. Lieb, Two theorems on the Hubbard model, *Phys. Rev. Lett.* 62 (10) (1989) 1201–1204.
- [49] N. Goldman, D. F. Urban, D. Bercioux, Topological phases for fermionic cold atoms on the Lieb lattice, *Phys. Rev. A* 83 (6) (2011) 063601.
- [50] A. Julku, S. Peotta, T. I. Vanhala, D.-H. Kim, P. Törmä, Geometric origin of superfluidity in the Lieb-lattice flat band, *Phys. Rev. Lett.* 117 (4) (2016) 045303.
- [51] C. Weeks, M. Franz, Topological insulators on the Lieb and perovskite lattices, *Phys. Rev. B* 82 (8) (2010) 085310.
- [52] H. Wang, Y. Yao, H. Song, X. Liu, Z. Chen, W. Chen, W. Zhu, Z. Li, J. Yang, Accelerating two-dimensional materials research via a universal interatomic potential and large language model agent (2025). [arXiv: 2506.07043](https://arxiv.org/abs/2506.07043).
- [53] T. Bray, The JavaScript Object Notation (JSON) data interchange format, RFC 8259, Internet Engineering Task Force (IETF) (2017).
- [54] G. Kresse, J. Furthmüller, Efficient iterative schemes for *ab initio* total-energy calculations using a plane-wave basis set, *Phys. Rev. B* 54 (16) (1996) 11169–11186.
- [55] G. Kresse, J. Furthmüller, Efficiency of *ab-initio* total energy calculations for metals and semiconductors using a plane-wave basis set, *Comput. Mater. Sci.* 6 (1) (1996) 15–50.

## Supporting Information

UniMatSim: A High-Throughput Materials Simulation Automation Framework Based on Universal Machine Learning Potentials

Yanjin Xiang, Yihan Nie, Yunzhi Gao, Haidi Wang\*, Wei Hu\*

\*Corresponding authors: haidi@hfut.edu.cn (Haidi Wang), whuustc@ustc.edu.cn (Wei Hu)

## S1. Cross-Validation and Model Stability Analysis

To improve the reliability of our screening, we fine-tuned the MatterSim potential, generating four independent model variants trained with distinct random seeds (4, 123, 2025, 8888). Each variant was used to run the complete high-throughput stability workflow—comprising structural optimization, elastic stability screening, phonon calculations, and a final stability assessment—on all candidate Lieb-lattice structures.

We then performed a systematic cross-validation of the predictions from the four models. The UpSet plot in Fig. S1 visualizes the agreement among models regarding phonon stability. The analysis reveals that only 393 materials were consistently predicted as stable by all four models. This consensus subset effectively filters out false positives arising from training stochasticity, yielding a high-confidence pool of candidates for subsequent first-principles validation.

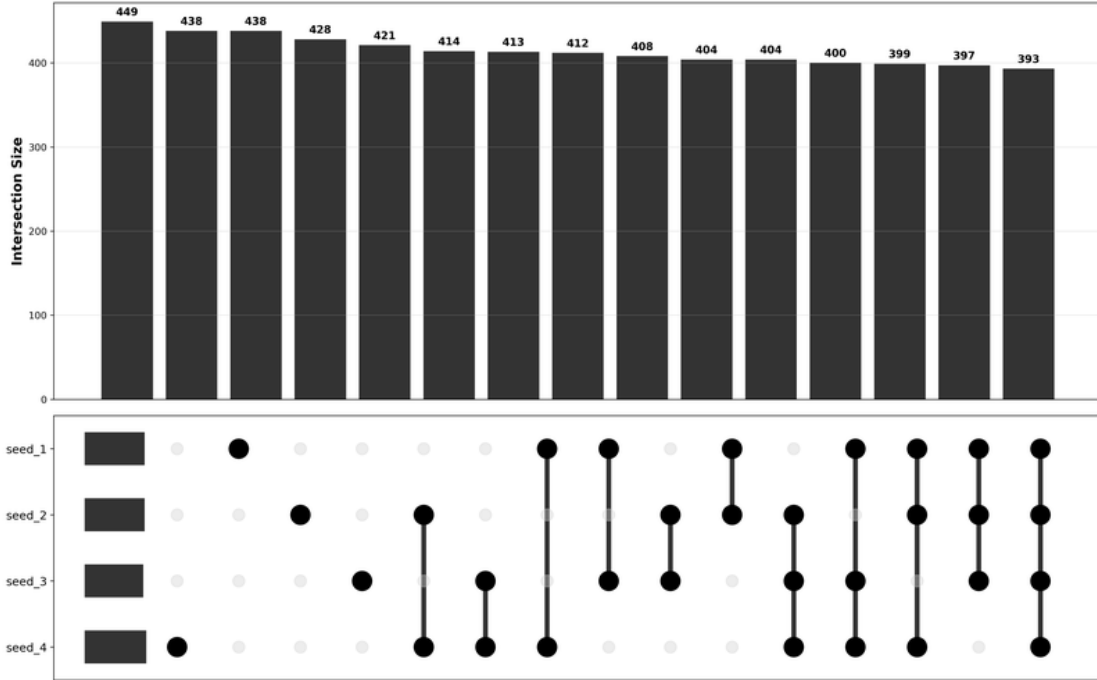


Figure S1: UpSet plot showing the overlap in phonon-stable materials identified by four independently fine-tuned MatterSim models. A total of 393 materials were predicted as stable by all four models.

This exercise confirms the robustness of UniMatSim for multi-model screening and illustrates how model ensembles can enhance the reliability of high-throughput computational pipelines.

## S2. Details of Density Functional Theory Calculation Parameters

All density functional theory (DFT) calculations were performed using the Vienna Ab initio Simulation Package (VASP)[54, 55] with the projector-augmented wave (PAW) method.

Initial structural relaxations used a plane-wave energy cutoff (ENCUT) of 520 eV and the `PREC = Accurate` setting. Electronic and ionic relaxations were considered converged when the energy change between steps fell below  $1 \times 10^{-5}$  eV (EDIFF) and the forces on all atoms were less than  $0.01$  eV/Å (EDIFFG), respectively. The exchange-correlation functional was the Becke-Roussel (BO) optimized functional, and spin polarization was included (`ISPIN = 2`). Brillouin-zone integration employed a  $9 \times 9 \times 1$   $\Gamma$ -centered k-point mesh with Gaussian or first-order Methfessel-Paxton smearing (`ISMEAR = 0` or `1`) and a smearing width of  $0.05$  eV (`SIGMA`).

Static self-consistent field calculations for final energies and densities used a finer  $13 \times 13 \times 1$  k-mesh and the tetrahedron method with Blöchl corrections (`ISMEAR = -5`) to improve accuracy for metallic and narrow-gap systems. The plane-wave cutoff, functional, and spin settings remained unchanged from the relaxation stage. Band structures were computed along the high-symmetry path  $\Gamma$ -M-K- $\Gamma$  using the same potential and cutoff, with Gaussian smearing (`ISMEAR = 0`) applied for smooth dispersion. A vacuum layer of at least  $15$  Å was added perpendicular to the layers to avoid spurious interactions between periodic images in these two-dimensional materials.

### S3. Summary of Crystallographic Parameters for Staggered-Magnetic Lieb Lattice Materials

Crystallographic parameters for all 59 identified staggered-magnetic Lieb-lattice materials are summarized here, including optimized lattice constants, unit-cell volumes, and space-group symmetries. All data were obtained from the final relaxed structures of the VASP calculations. The materials crystallize in the two-dimensional layered Lieb-lattice structure, modeled with a vacuum layer along the *c* axis. Variations in the lattice parameters reflect the influence of different chemical compositions. Space-group analysis shows that the symmetry is highly consistent: 58 of the 59 compounds adopt the P-4m2 space group, with Fe<sub>2</sub>Te<sub>4</sub>Ru being the sole exception (space group Cmm2).

Table S1: Basic crystallographic parameters of the 59 staggered-magnetic Lieb-lattice materials

ID	Formula	Lattice	Volume	Atoms	Space Group
1	Co <sub>2</sub> CuSe <sub>4</sub>	$a = 5.402, b = 5.402, c = 19.985$	583.16	7	P-42m
2	Co <sub>2</sub> WSe <sub>4</sub>	$a = 5.487, b = 5.487, c = 19.985$	601.69	7	P-42m
3	CrFe <sub>2</sub> S <sub>4</sub>	$a = 5.257, b = 5.257, c = 19.985$	552.23	7	P-42m
4	CrFe <sub>2</sub> Se <sub>4</sub>	$a = 5.416, b = 5.416, c = 19.985$	586.31	7	P-42m
5	Fe <sub>2</sub> CuTe <sub>4</sub>	$a = 5.246, b = 5.246, c = 19.985$	550.02	7	P-42m
6	Fe <sub>2</sub> MoSe <sub>4</sub>	$a = 5.417, b = 5.417, c = 19.985$	586.45	7	P-42m
7	Fe <sub>2</sub> NiS <sub>4</sub>	$a = 5.039, b = 5.039, c = 19.985$	507.42	7	P-42m
8	Fe <sub>2</sub> NiSe <sub>4</sub>	$a = 5.278, b = 5.278, c = 19.985$	556.68	7	P-42m
9	Fe <sub>2</sub> OsSe <sub>4</sub>	$a = 5.325, b = 5.325, c = 19.985$	566.71	7	P-42m
10	Fe <sub>2</sub> PtSe <sub>4</sub>	$a = 5.359, b = 5.359, c = 19.985$	574.01	7	P-42m
11	Fe <sub>2</sub> ReSe <sub>4</sub>	$a = 5.412, b = 5.412, c = 19.985$	585.40	7	P-42m
12	Fe <sub>2</sub> ReTe <sub>4</sub>	$a = 5.542, b = 5.542, c = 19.985$	613.85	7	P-42m
13	Fe <sub>2</sub> TcP <sub>4</sub>	$a = 5.446, b = 5.446, c = 19.985$	592.80	7	P-42m
14	Fe <sub>2</sub> TcS <sub>4</sub>	$a = 5.289, b = 5.288, c = 19.985$	558.94	7	P-42m
15	Fe <sub>2</sub> TcSe <sub>4</sub>	$a = 5.419, b = 5.419, c = 19.985$	586.90	7	P-42m
16	Fe <sub>2</sub> TcTe <sub>4</sub>	$a = 5.595, b = 5.595, c = 19.985$	625.54	7	P-42m
17	Fe <sub>2</sub> Te <sub>4</sub> Pt	$a = 5.309, b = 5.309, c = 19.985$	563.38	7	P-42m
18	Fe <sub>2</sub> Te <sub>4</sub> Rh	$a = 5.574, b = 5.574, c = 19.985$	620.91	7	P-42m
19	Fe <sub>2</sub> Te <sub>4</sub> Ru	$a = 5.551, b = 5.551, c = 19.985$	615.46	7	Cmm2
20	Fe <sub>2</sub> WSe <sub>4</sub>	$a = 5.556, b = 5.556, c = 19.985$	616.90	7	P-42m
21	HfMn <sub>2</sub> S <sub>4</sub>	$a = 6.123, b = 6.123, c = 19.985$	749.16	7	P-42m
22	HfMn <sub>2</sub> Se <sub>4</sub>	$a = 6.272, b = 6.272, c = 19.985$	786.15	7	P-42m
23	HfMn <sub>2</sub> Te <sub>4</sub>	$a = 6.503, b = 6.503, c = 19.985$	845.06	7	P-42m
24	Mn <sub>2</sub> CrSe <sub>4</sub>	$a = 5.852, b = 5.852, c = 19.985$	684.39	7	P-42m
25	Mn <sub>2</sub> CrTe <sub>4</sub>	$a = 6.082, b = 6.082, c = 19.985$	739.32	7	P-42m
26	Mn <sub>2</sub> CuS <sub>4</sub>	$a = 5.477, b = 5.477, c = 19.985$	599.54	7	P-42m
27	Mn <sub>2</sub> MoS <sub>4</sub>	$a = 5.654, b = 5.654, c = 19.985$	638.94	7	P-42m
28	Mn <sub>2</sub> MoSe <sub>4</sub>	$a = 5.778, b = 5.778, c = 19.985$	667.16	7	P-42m
29	Mn <sub>2</sub> NbS <sub>4</sub>	$a = 5.828, b = 5.828, c = 19.985$	678.84	7	P-42m
30	Mn <sub>2</sub> NbSe <sub>4</sub>	$a = 5.982, b = 5.982, c = 19.985$	715.13	7	P-42m
31	Mn <sub>2</sub> NbTe <sub>4</sub>	$a = 6.212, b = 6.212, c = 19.985$	771.17	7	P-42m
32	Mn <sub>2</sub> NiTe <sub>4</sub>	$a = 5.412, b = 5.412, c = 19.985$	585.36	7	P-42m
33	Mn <sub>2</sub> OsS <sub>4</sub>	$a = 5.280, b = 5.280, c = 19.985$	557.21	7	P-42m
34	Mn <sub>2</sub> OsSe <sub>4</sub>	$a = 5.377, b = 5.377, c = 19.985$	577.80	7	P-42m
35	Mn <sub>2</sub> ReSe <sub>4</sub>	$a = 5.571, b = 5.572, c = 19.985$	620.36	7	P-42m
36	Mn <sub>2</sub> RuS <sub>4</sub>	$a = 5.290, b = 5.286, c = 19.985$	558.83	7	P-42m
37	Mn <sub>2</sub> RuSe <sub>4</sub>	$a = 5.430, b = 5.430, c = 19.985$	589.31	7	P-42m
38	Mn <sub>2</sub> TcSe <sub>4</sub>	$a = 5.580, b = 5.580, c = 19.985$	622.37	7	P-42m
39	Mn <sub>2</sub> TcTe <sub>4</sub>	$a = 5.790, b = 5.790, c = 19.985$	670.06	7	P-42m
40	Mn <sub>2</sub> Te <sub>4</sub> Mo	$a = 5.970, b = 5.970, c = 19.985$	712.29	7	P-42m
41	Mn <sub>2</sub> Te <sub>4</sub> Pd	$a = 5.482, b = 5.482, c = 19.985$	600.50	7	P-42m
42	Mn <sub>2</sub> VS <sub>4</sub>	$a = 5.670, b = 5.670, c = 19.985$	642.53	7	P-42m
43	Mn <sub>2</sub> VSe <sub>4</sub>	$a = 5.854, b = 5.854, c = 19.985$	684.94	7	P-42m
44	Mn <sub>2</sub> VTe <sub>4</sub>	$a = 6.099, b = 6.099, c = 19.985$	743.35	7	P-42m

Table S1: Basic crystallographic parameters of the 59 staggered-magnetic Lieb-lattice materials (continued)

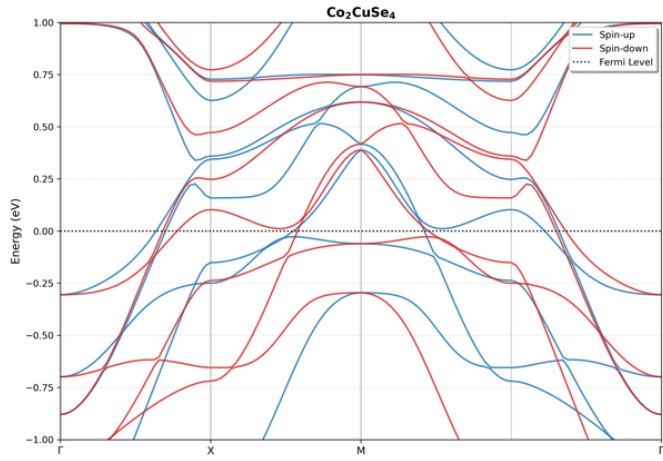
ID	Formula	Lattice	Volume	Atoms	Space Group
45	Mn <sub>2</sub> WS <sub>4</sub>	$a = 5.656, b = 5.656, c = 19.985$	639.33	7	P-42m
46	TaCo <sub>2</sub> Se <sub>4</sub>	$a = 5.653, b = 5.653, c = 19.985$	638.69	7	P-42m
47	TaCo <sub>2</sub> Te <sub>4</sub>	$a = 5.873, b = 5.873, c = 19.985$	689.40	7	P-42m
48	TaMn <sub>2</sub> S <sub>4</sub>	$a = 5.837, b = 5.836, c = 19.985$	680.82	7	P-42m
49	TaMn <sub>2</sub> Se <sub>4</sub>	$a = 5.981, b = 5.981, c = 19.985$	714.89	7	P-42m
50	TiCo <sub>2</sub> S <sub>4</sub>	$a = 5.445, b = 5.445, c = 19.985$	592.53	7	P-42m
51	TiCo <sub>2</sub> Se <sub>4</sub>	$a = 5.602, b = 5.600, c = 19.985$	626.92	7	P-42m
52	TiFe <sub>2</sub> S <sub>4</sub>	$a = 5.614, b = 5.614, c = 19.985$	629.87	7	P-42m
53	TiMn <sub>2</sub> S <sub>4</sub>	$a = 5.930, b = 5.930, c = 19.985$	702.87	7	P-42m
54	TiMn <sub>2</sub> Te <sub>4</sub>	$a = 6.343, b = 6.343, c = 19.985$	804.11	7	P-42m
55	VCo <sub>2</sub> S <sub>4</sub>	$a = 5.310, b = 5.310, c = 19.985$	563.40	7	P-42m
56	VFe <sub>2</sub> S <sub>4</sub>	$a = 5.243, b = 5.242, c = 19.985$	549.31	7	P-42m
57	ZnFe <sub>2</sub> S <sub>4</sub>	$a = 5.353, b = 5.353, c = 19.985$	572.62	7	P-42m
58	ZnFe <sub>2</sub> Se <sub>4</sub>	$a = 5.451, b = 5.451, c = 19.985$	593.78	7	P-42m
59	ZrMn <sub>2</sub> Te <sub>4</sub>	$a = 6.519, b = 6.519, c = 19.985$	849.34	7	P-42m

#### S4. Complete Atlas of Band Structures for Staggered-Spin Lieb Lattice Materials

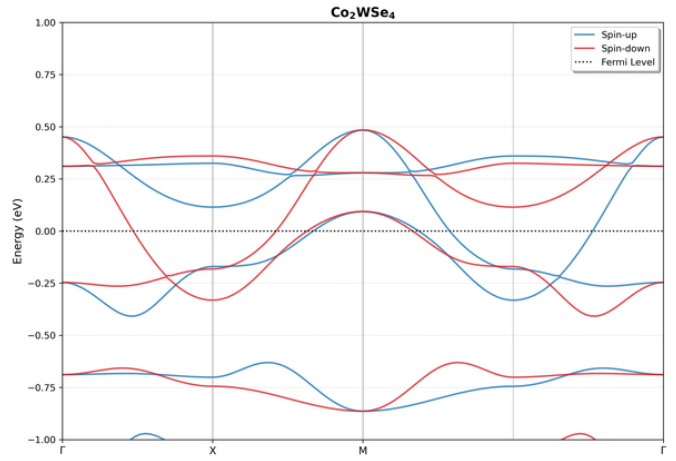
This section presents the full set of DFT-calculated band structures for the 59 Lieb-lattice materials identified by our high-throughput screening as exhibiting staggered-spin magnetic bands. These candidates were selected from an initial pool of 393 structures validated by multi-model cross-validation (employing four MatterSim models fine-tuned with distinct random seeds: 42, 123, 2025, 8888). All band structures were computed with spin-polarized DFT, highlighting their characteristic spin splitting and potential relevance to spintronics and magnetic quantum phenomena. To aid comparison, the materials are grouped logically by their chemical composition.

### S4.0.1. Cobalt-based Lieb Lattice Materials

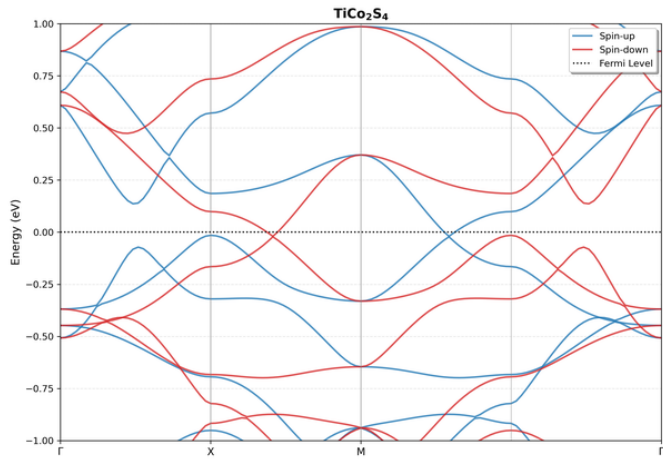
Cobalt-based Lieb lattices display a range of magnetic behaviors stemming from the partially filled 3d orbitals of Co. This subgroup includes various chalcogenide and pnictide compounds.



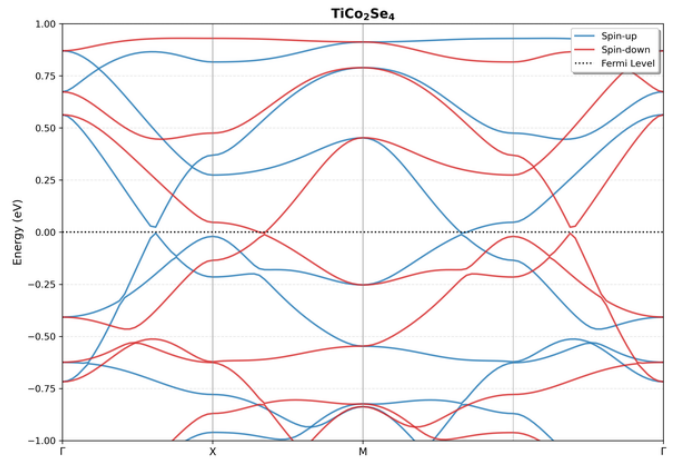
Spin-polarized band structure of  $\text{Co}_2\text{CuSe}_4$ .



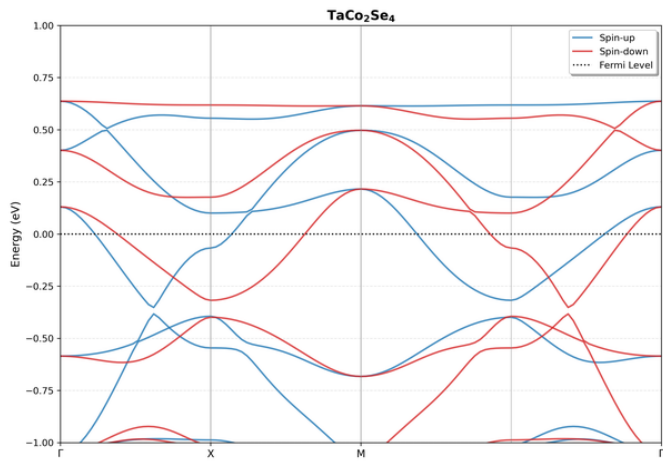
Spin-polarized band structure of  $\text{Co}_2\text{WSe}_4$ .



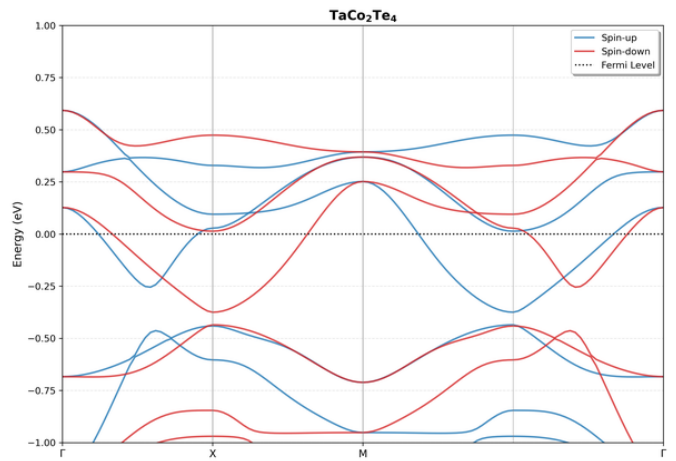
Spin-polarized band structure of  $\text{TiCo}_2\text{S}_4$ .



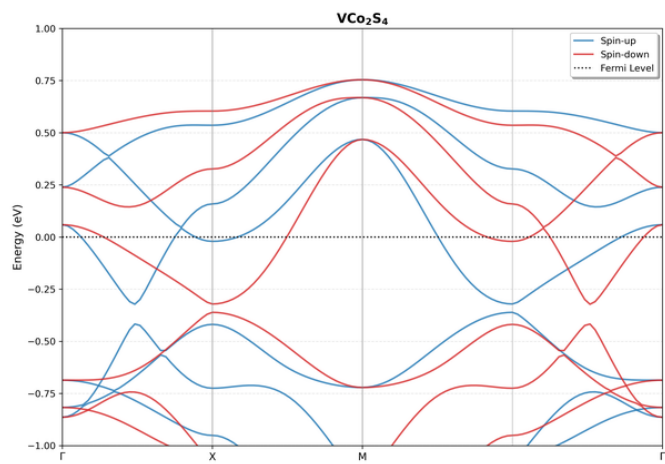
Spin-polarized band structure of  $\text{TiCo}_2\text{Se}_4$ .



Spin-polarized band structure of  $\text{TaCo}_2\text{Se}_4$ .



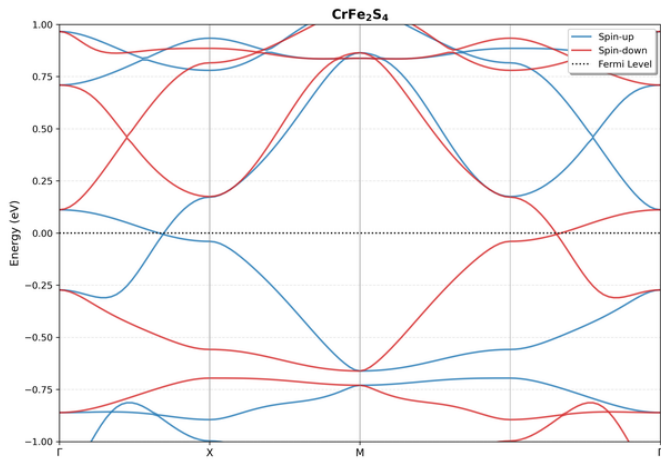
Spin-polarized band structure of  $\text{TaCo}_2\text{Te}_4$ .



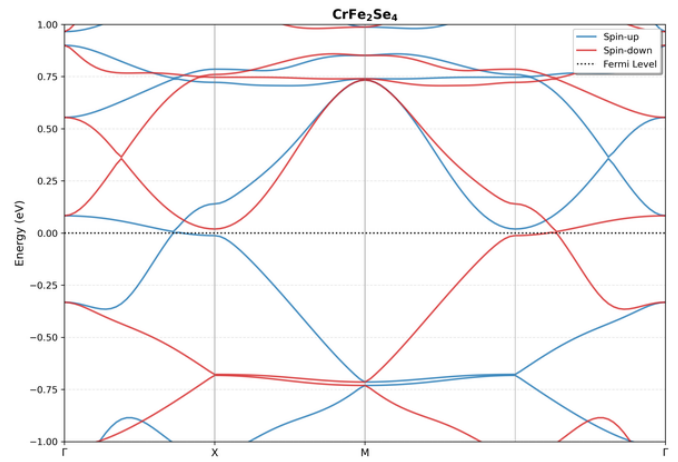
Spin-polarized band structure of VCo<sub>2</sub>S<sub>4</sub>.

#### S4.0.2. Cr-Fe Mixed Lieb Lattice Materials

The combination of Cr and Fe within the Lieb lattice configuration yields materials exhibiting particularly strong magnetic exchange interactions, which typically result in large spin splitting in the electronic band structure.



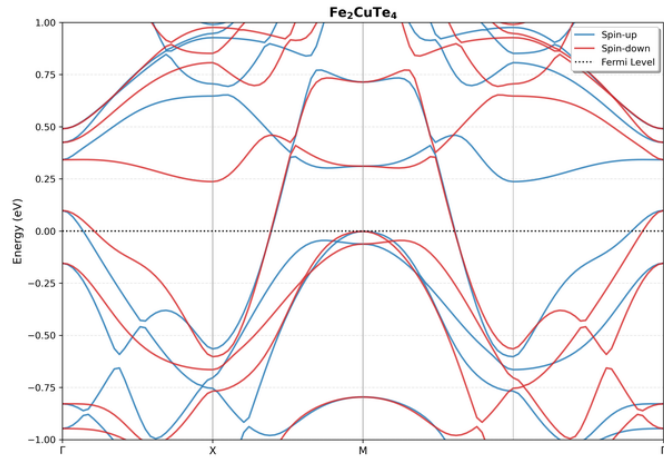
Spin-polarized band structure of CrFe<sub>2</sub>S<sub>4</sub>.



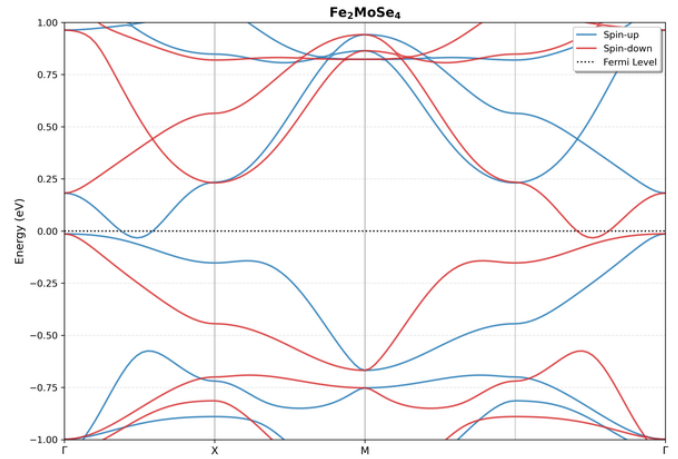
Spin-polarized band structure of CrFe<sub>2</sub>Se<sub>4</sub>.

### S4.0.3. Iron-based Lieb Lattice Materials

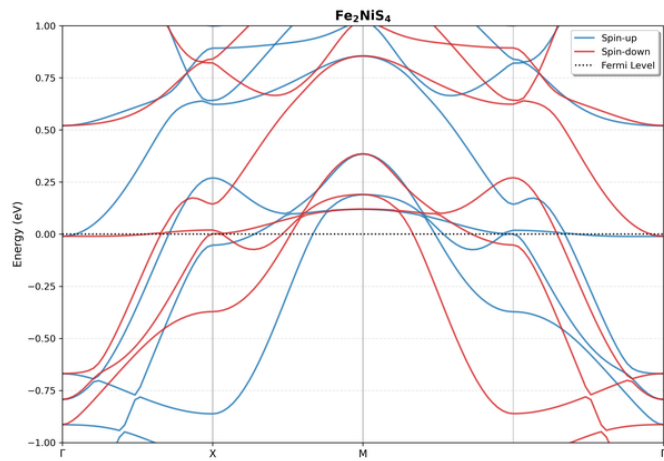
Iron-based Lieb lattices constitute a significant portion of the discovered materials, exhibiting diverse electronic and magnetic properties across various compositions.



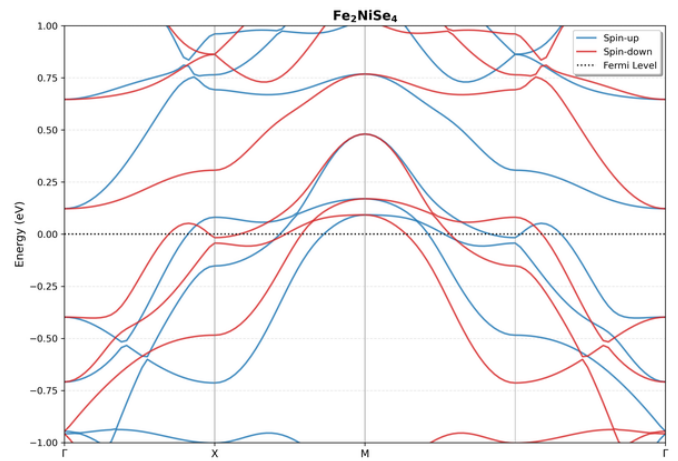
Spin-polarized band structure of  $\text{Fe}_2\text{CuTe}_4$ .



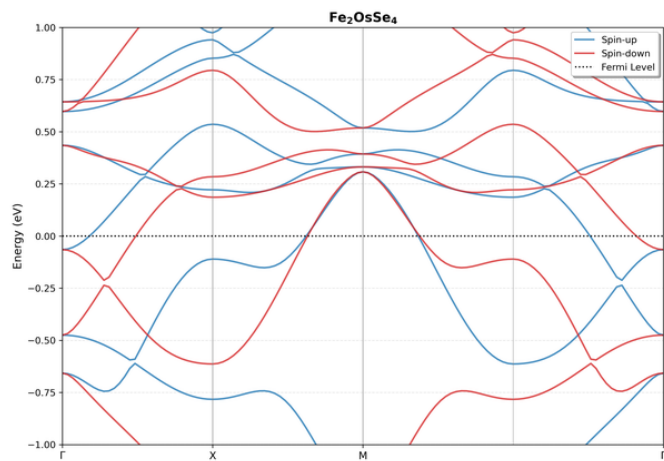
Spin-polarized band structure of  $\text{Fe}_2\text{MoSe}_4$ .



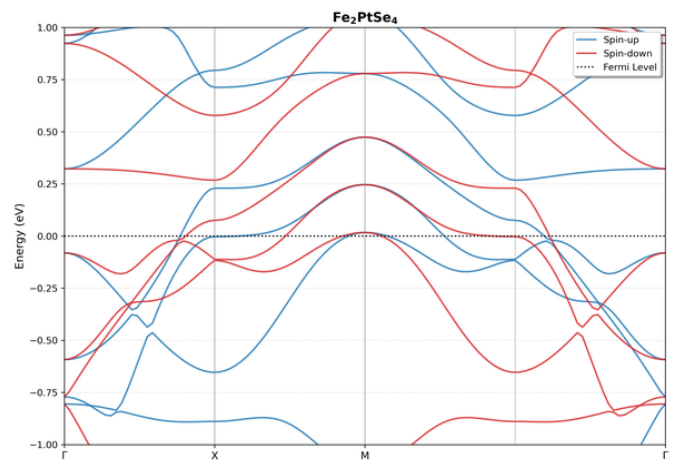
Spin-polarized band structure of  $\text{Fe}_2\text{NiS}_4$ .



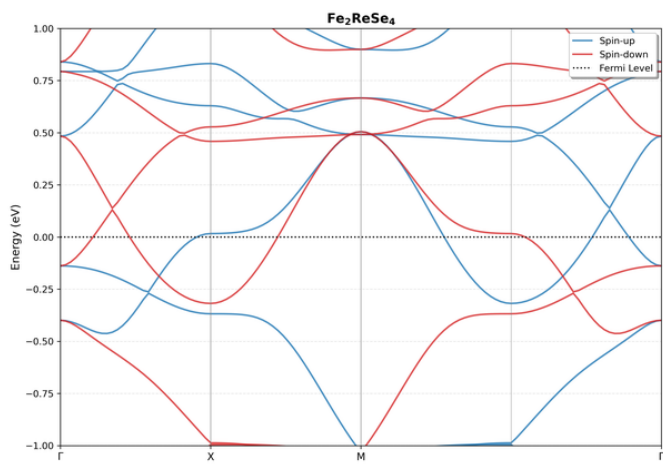
Spin-polarized band structure of  $\text{Fe}_2\text{NiSe}_4$ .



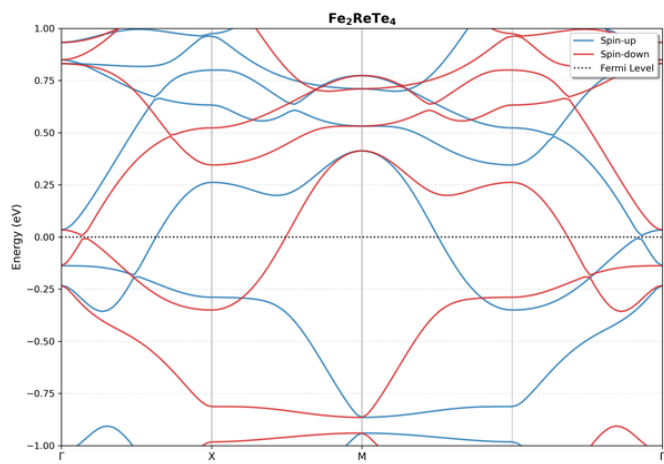
Spin-polarized band structure of  $\text{Fe}_2\text{OsSe}_4$ .



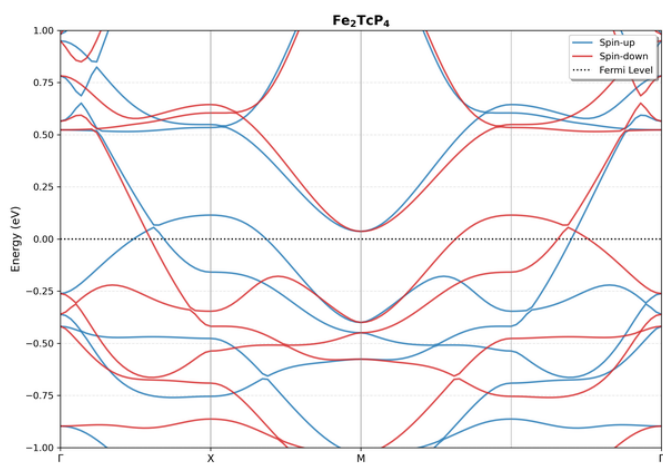
Spin-polarized band structure of  $\text{Fe}_2\text{PtSe}_4$ .



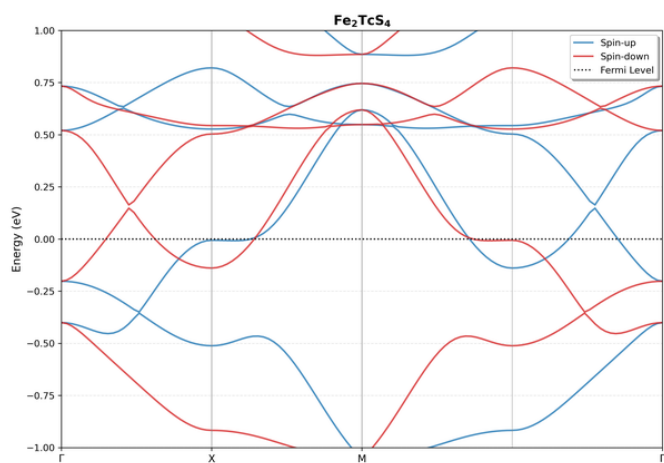
Spin-polarized band structure of  $\text{Fe}_2\text{ReSe}_4$ .



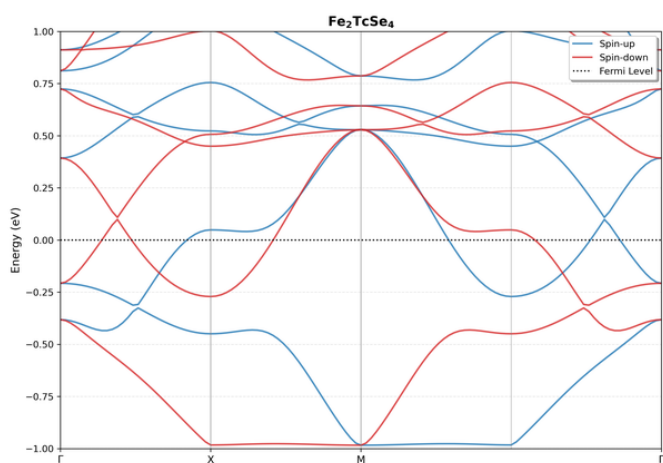
Spin-polarized band structure of  $\text{Fe}_2\text{ReTe}_4$ .



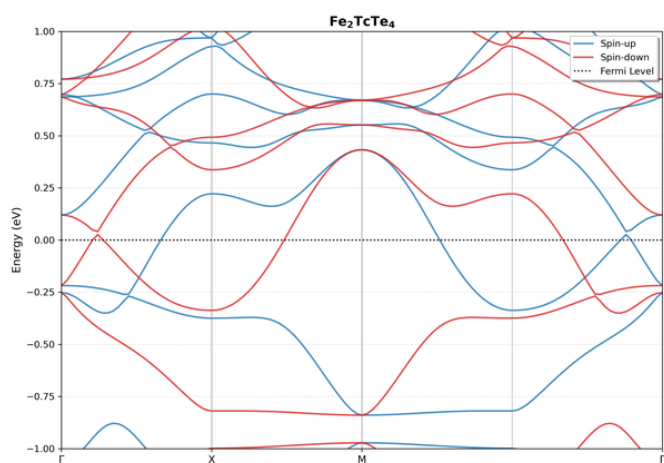
Spin-polarized band structure of  $\text{Fe}_2\text{TcP}_4$ .



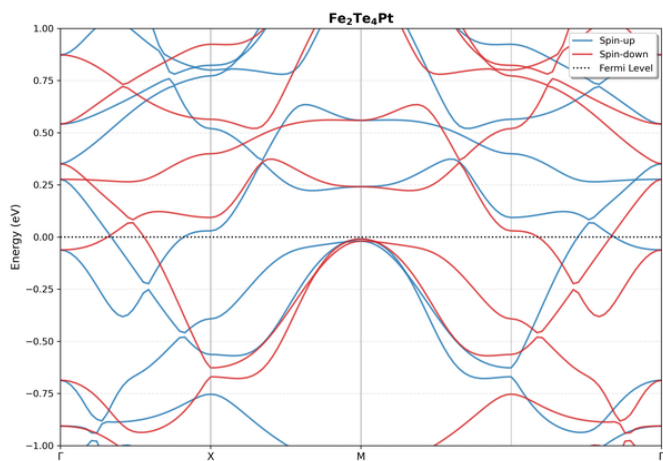
Spin-polarized band structure of  $\text{Fe}_2\text{TcS}_4$ .



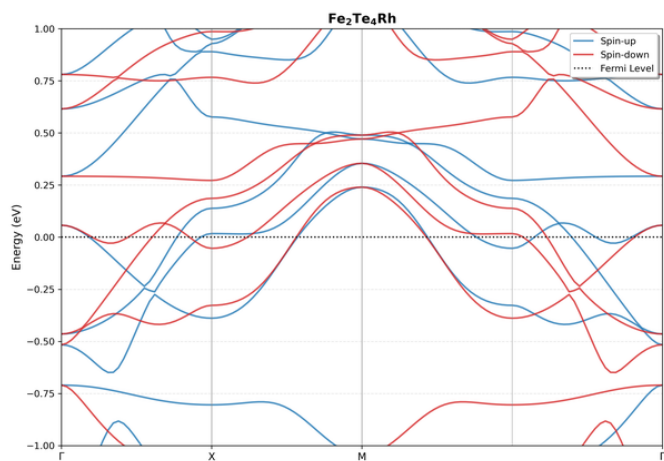
Spin-polarized band structure of  $\text{Fe}_2\text{TcSe}_4$ .



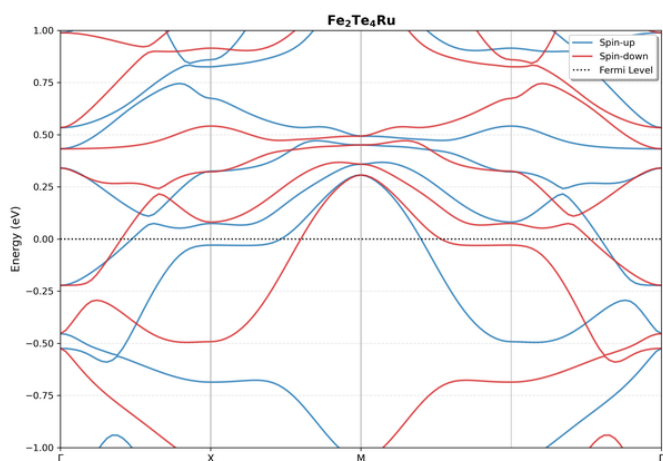
Spin-polarized band structure of  $\text{Fe}_2\text{TcTe}_4$ .



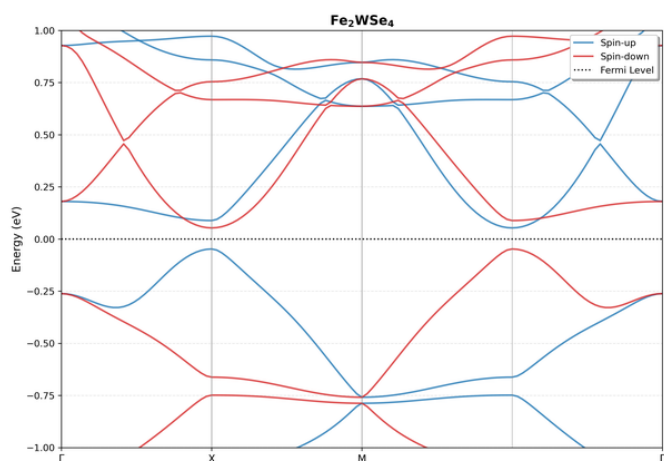
Spin-polarized band structure of  $\text{Fe}_2\text{Te}_4\text{Pt}$ .



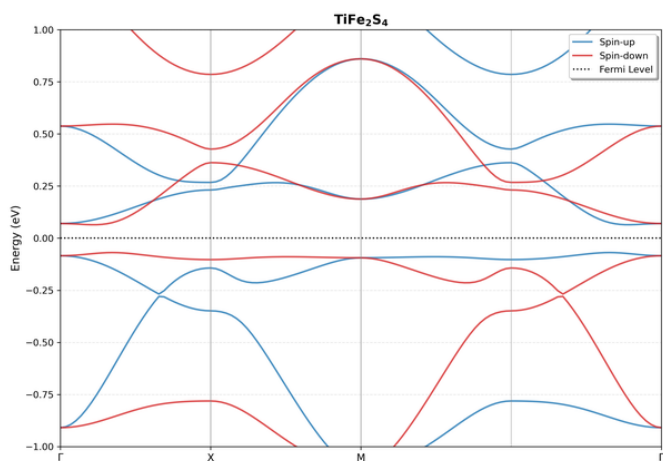
Spin-polarized band structure of  $\text{Fe}_2\text{Te}_4\text{Rh}$ .



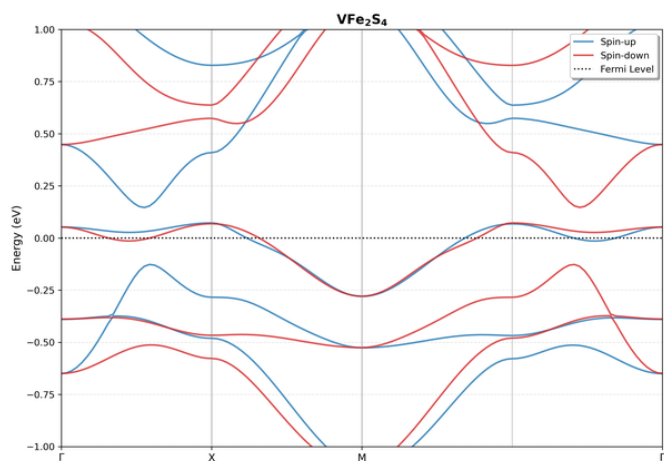
Spin-polarized band structure of  $\text{Fe}_2\text{Te}_4\text{Ru}$ .



Spin-polarized band structure of  $\text{Fe}_2\text{WSe}_4$ .



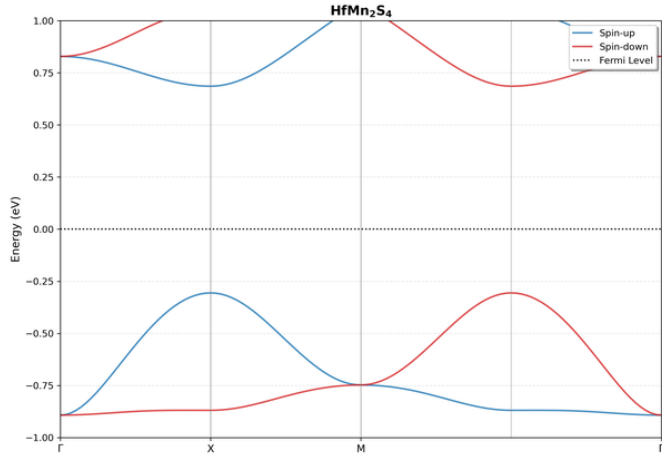
Spin-polarized band structure of  $\text{TiFe}_2\text{S}_4$ .



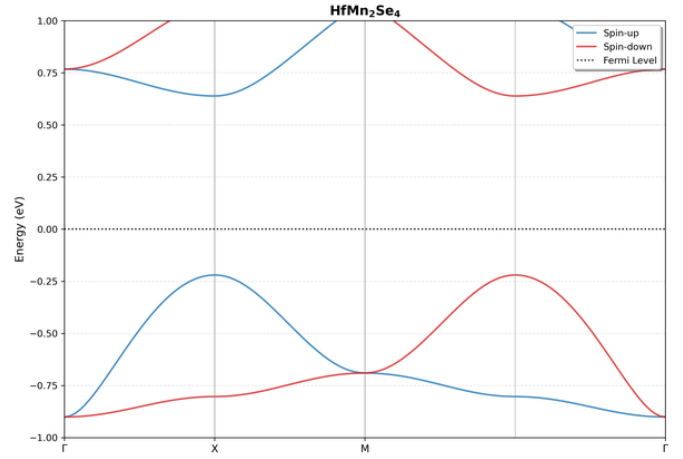
Spin-polarized band structure of  $\text{VFe}_2\text{S}_4$ .

#### S4.0.4. Manganese-based Lieb Lattice Materials

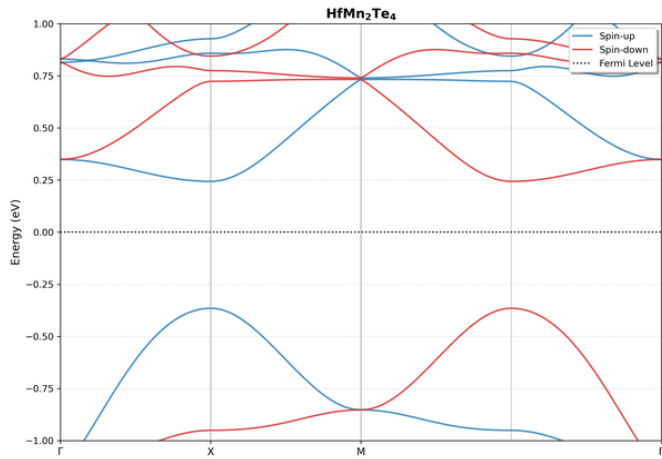
Manganese-based compounds form the largest subgroup among the identified materials. The high-spin  $d^5$  configuration of  $Mn^{2+}$  gives rise to strong magnetic exchange interactions and diverse spin-polarized electronic properties.



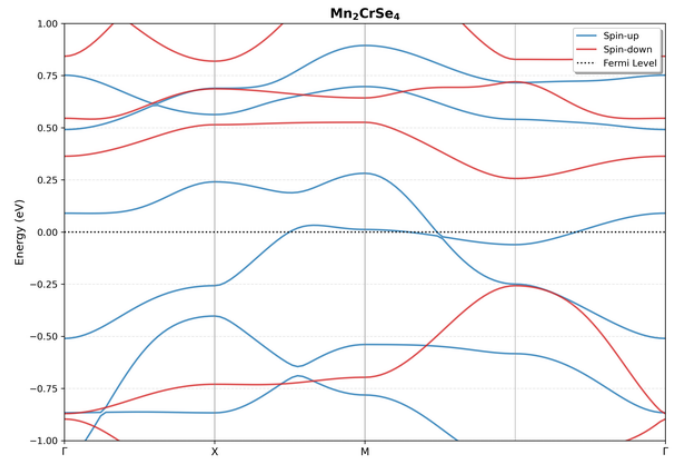
Spin-polarized band structure of  $HfMn_2S_4$ .



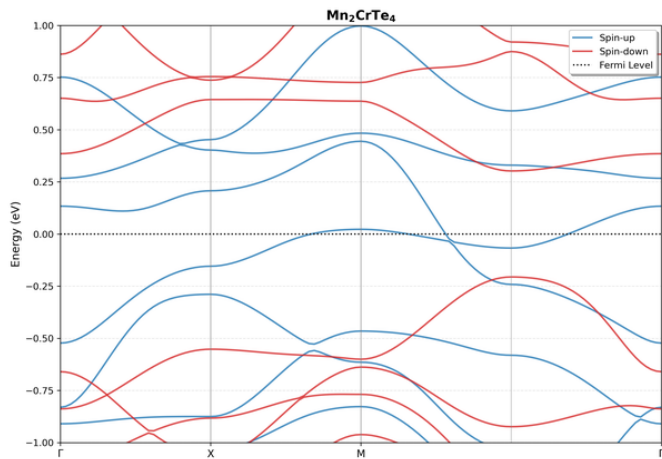
Spin-polarized band structure of  $HfMn_2Se_4$ .



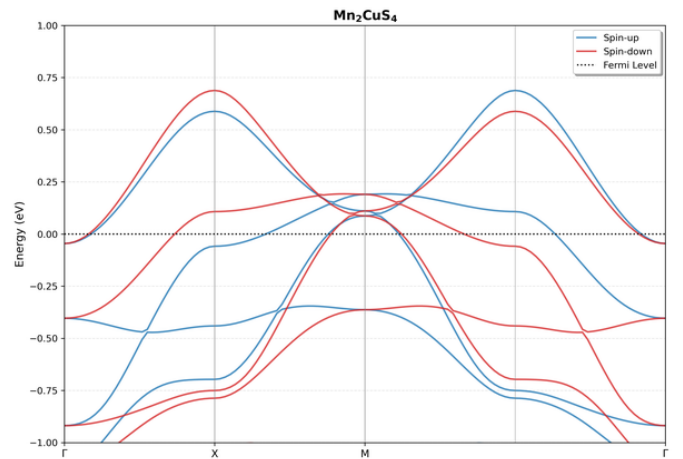
Spin-polarized band structure of  $HfMn_2Te_4$ .



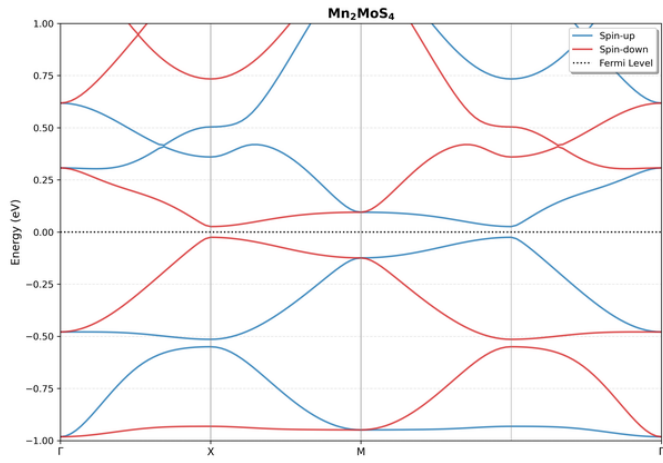
Spin-polarized band structure of  $Mn_2CrSe_4$ .



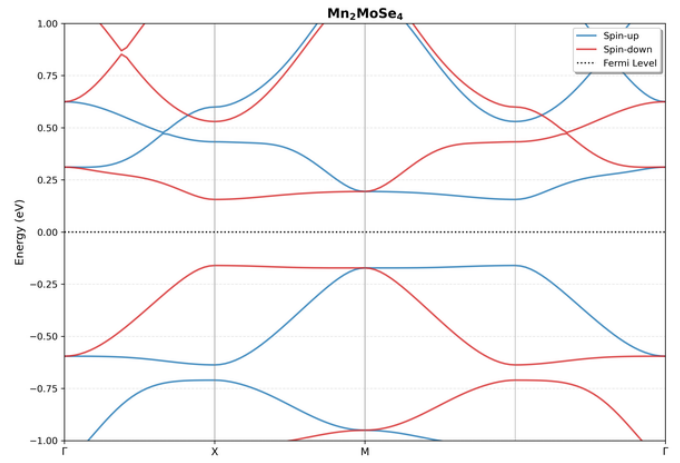
Spin-polarized band structure of  $Mn_2CrTe_4$ .



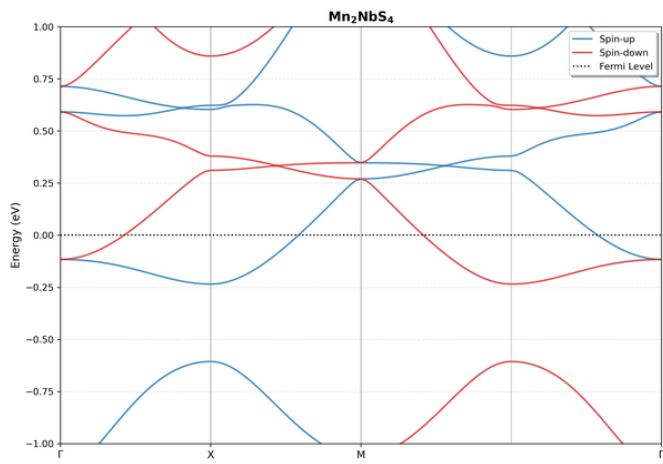
Spin-polarized band structure of  $Mn_2CuS_4$ .



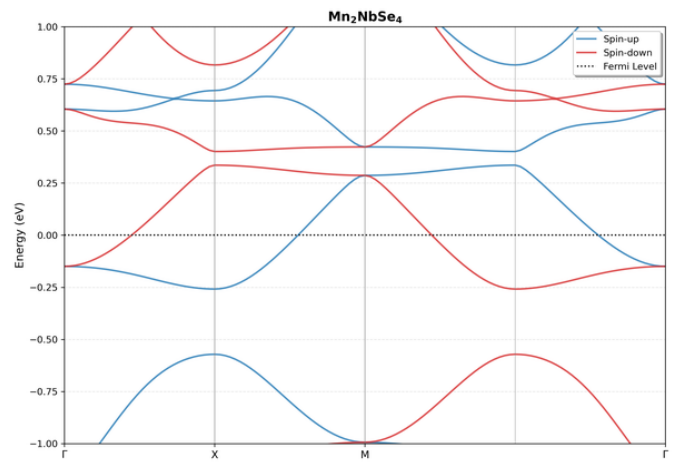
Spin-polarized band structure of  $\text{Mn}_2\text{MoS}_4$ .



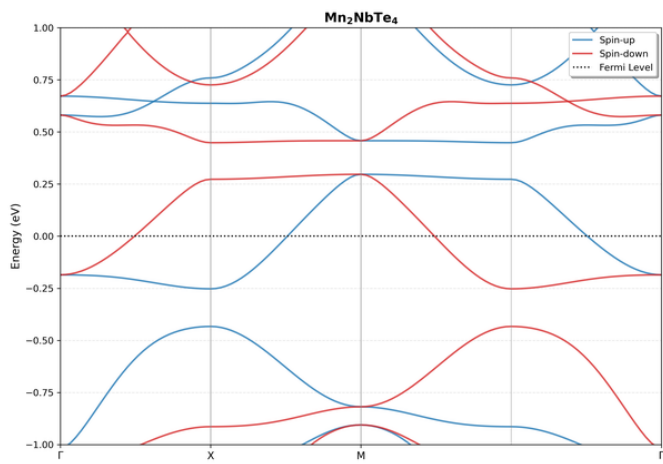
Spin-polarized band structure of  $\text{Mn}_2\text{MoSe}_4$ .



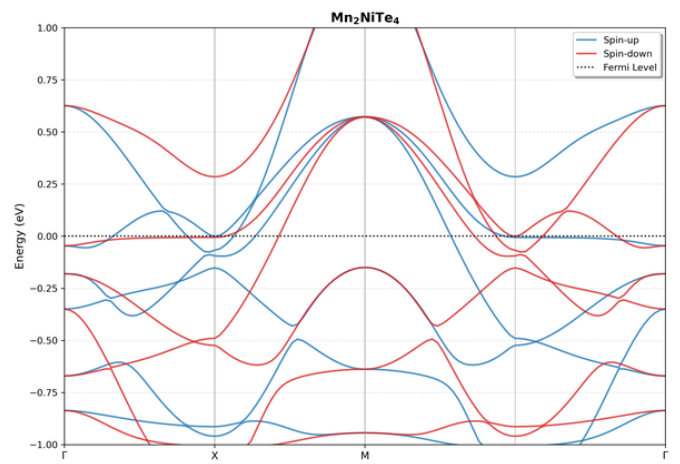
Spin-polarized band structure of  $\text{Mn}_2\text{NbS}_4$ .



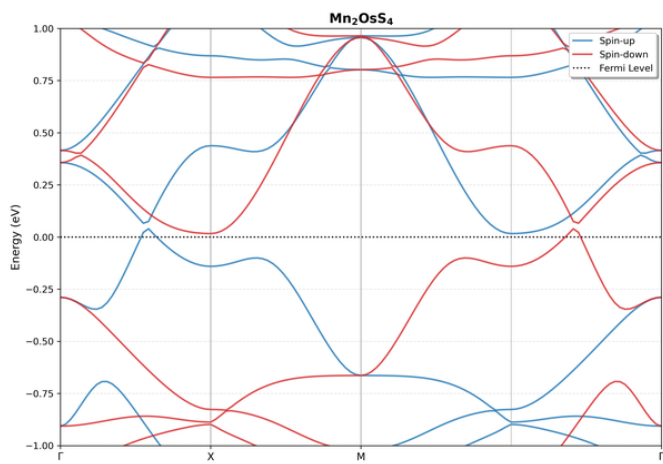
Spin-polarized band structure of  $\text{Mn}_2\text{NbSe}_4$ .



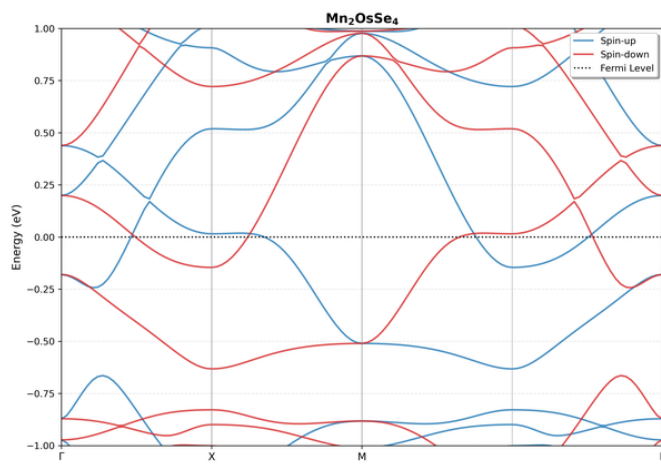
Spin-polarized band structure of  $\text{Mn}_2\text{NbTe}_4$ .



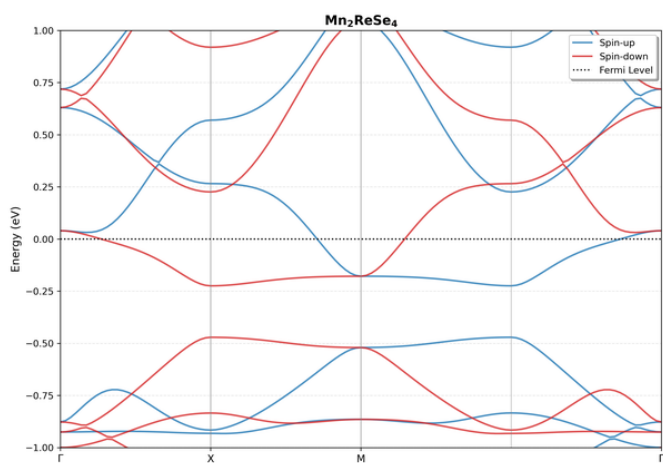
Spin-polarized band structure of  $\text{Mn}_2\text{NiTe}_4$ .



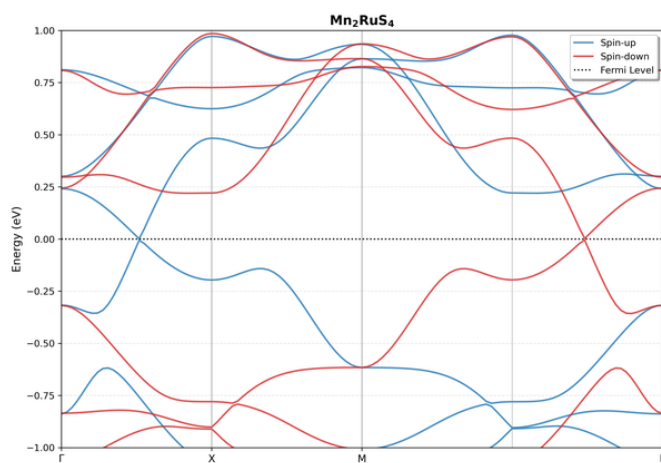
Spin-polarized band structure of  $\text{Mn}_2\text{OsS}_4$ .



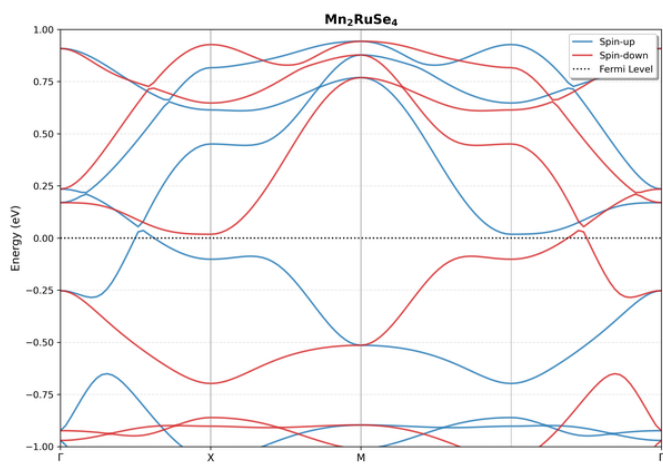
Spin-polarized band structure of  $\text{Mn}_2\text{OsSe}_4$ .



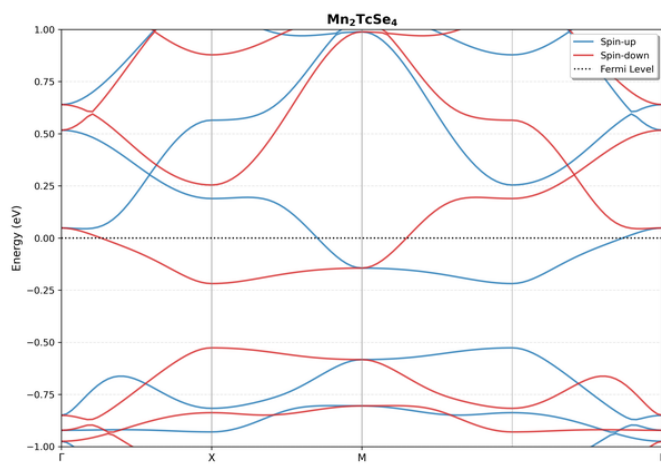
Spin-polarized band structure of  $\text{Mn}_2\text{ReSe}_4$ .



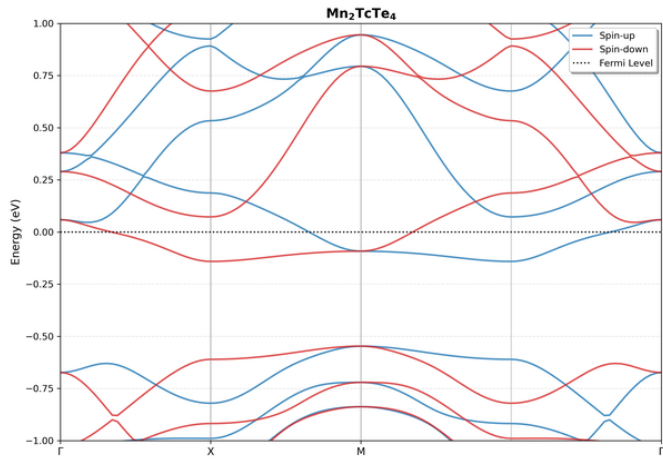
Spin-polarized band structure of  $\text{Mn}_2\text{RuS}_4$ .



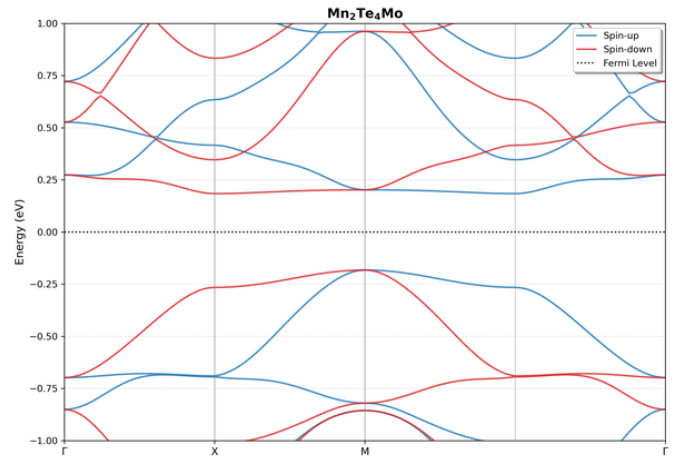
Spin-polarized band structure of  $\text{Mn}_2\text{RuSe}_4$ .



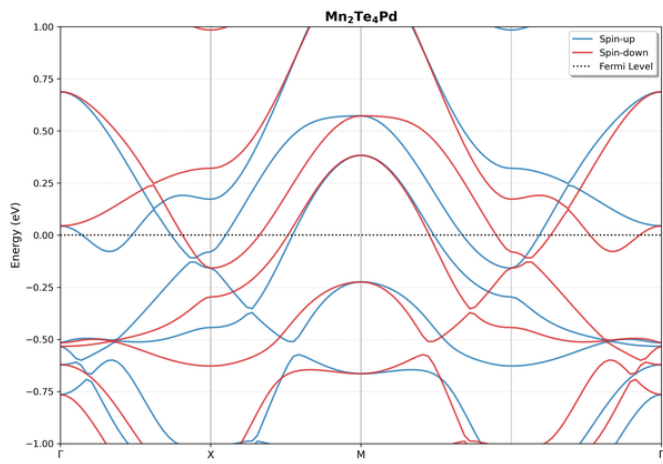
Spin-polarized band structure of  $\text{Mn}_2\text{TcSe}_4$ .



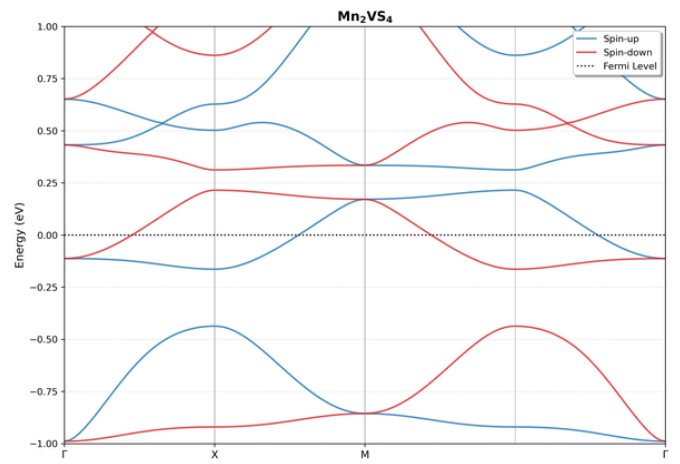
Spin-polarized band structure of  $\text{Mn}_2\text{TcTe}_4$ .



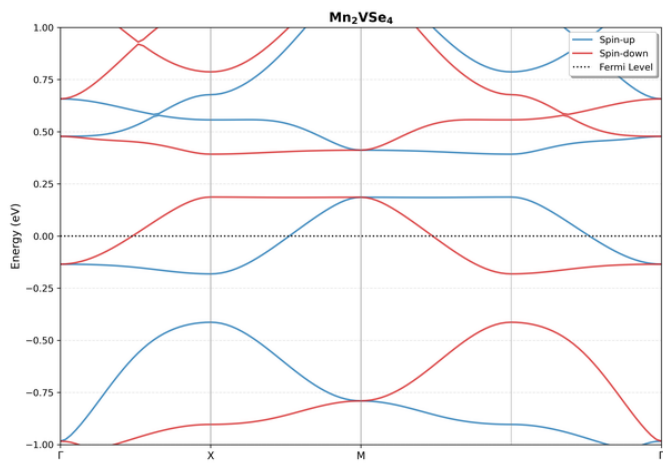
Spin-polarized band structure of  $\text{Mn}_2\text{Te}_4\text{Mo}$ .



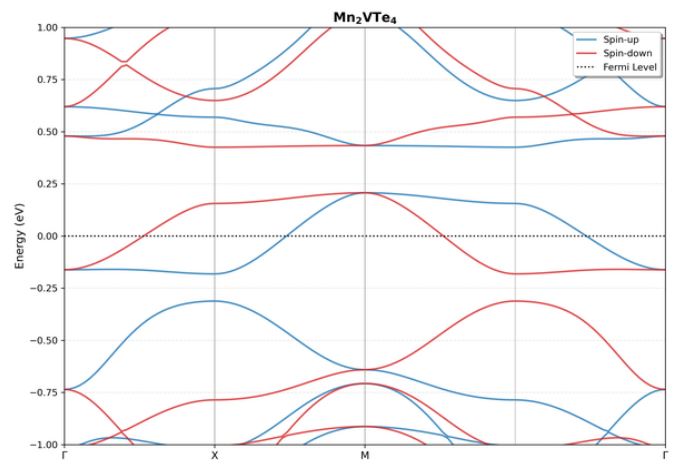
Spin-polarized band structure of  $\text{Mn}_2\text{Te}_4\text{Pd}$ .



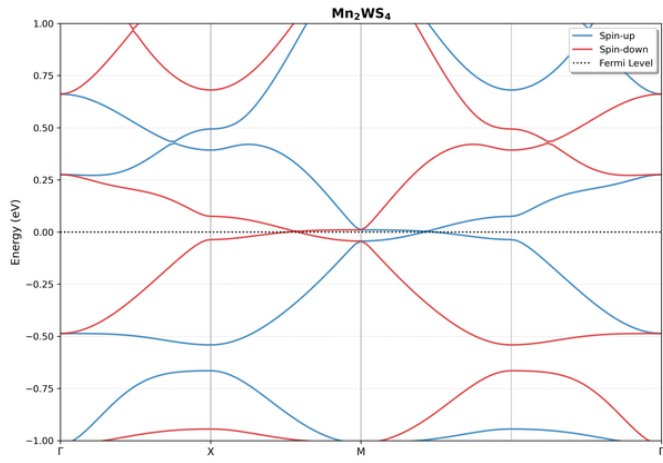
Spin-polarized band structure of  $\text{Mn}_2\text{VS}_4$ .



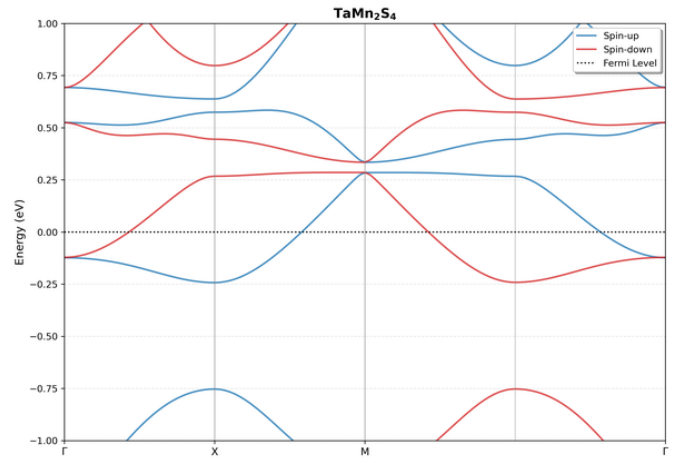
Spin-polarized band structure of  $\text{Mn}_2\text{VSe}_4$ .



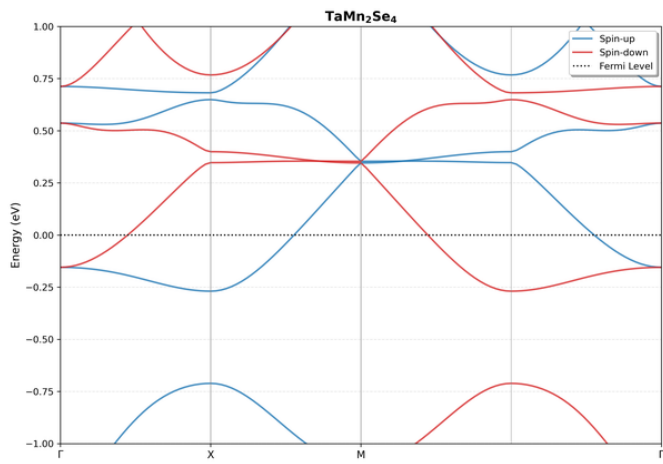
Spin-polarized band structure of  $\text{Mn}_2\text{VTe}_4$ .



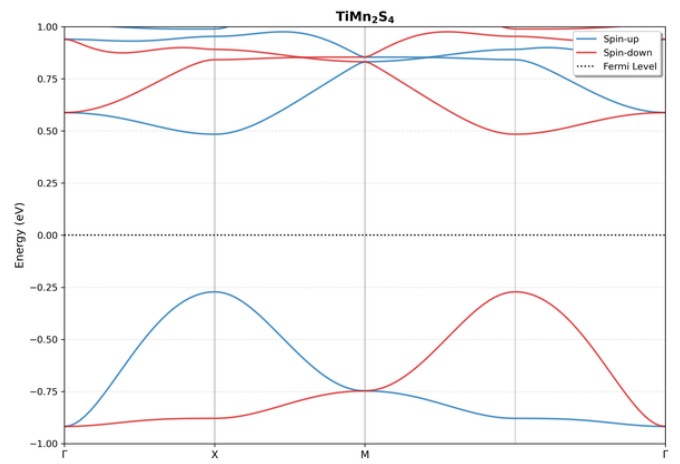
Spin-polarized band structure of  $\text{Mn}_2\text{WS}_4$ .



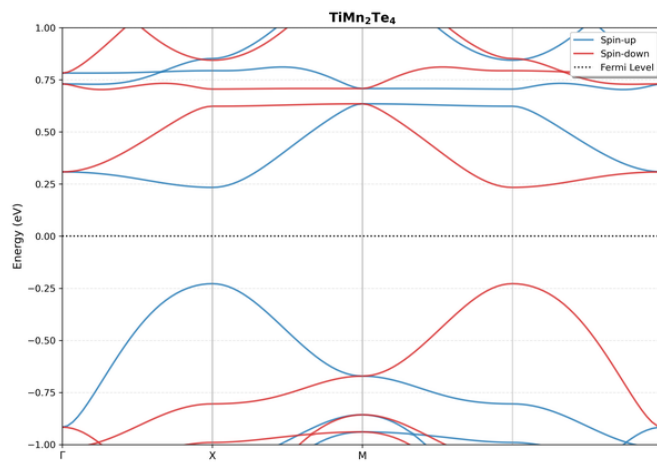
Spin-polarized band structure of  $\text{TaMn}_2\text{S}_4$ .



Spin-polarized band structure of  $\text{TaMn}_2\text{Se}_4$ .



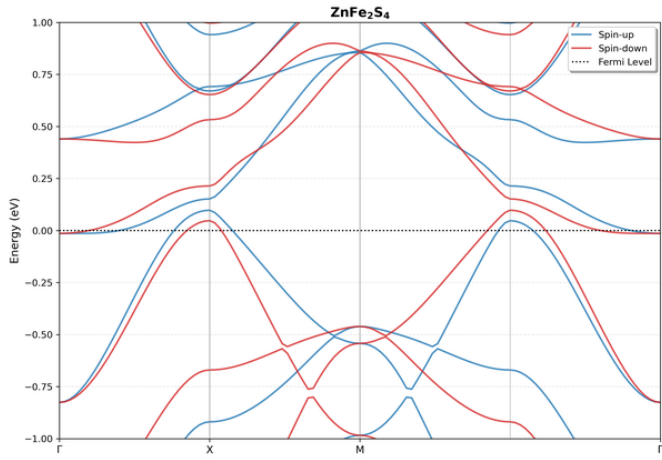
Spin-polarized band structure of  $\text{TiMn}_2\text{S}_4$ .



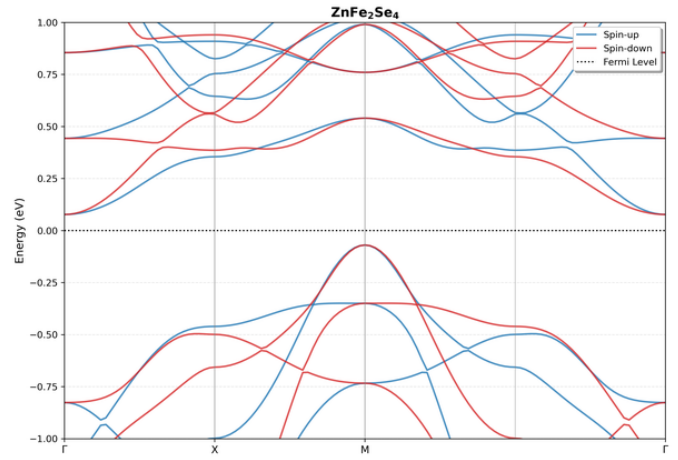
Spin-polarized band structure of  $\text{TiMn}_2\text{Te}_4$ .

#### S4.0.5. Other Lieb Lattice Materials

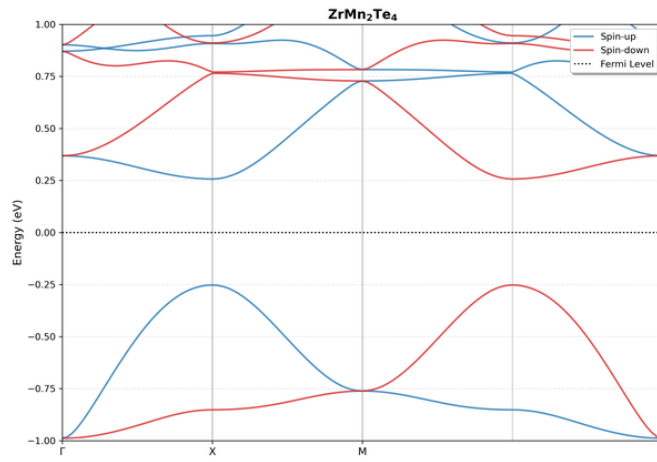
This subgroup comprises Zn- and Zr-based compounds, illustrating the behavior of non-magnetic or weakly magnetic constituents in the Lieb-lattice framework.



Spin-polarized band structure of ZnFe<sub>2</sub>S<sub>4</sub>.



Spin-polarized band structure of ZnFe<sub>2</sub>Se<sub>4</sub>.



Spin-polarized band structure of ZrMn<sub>2</sub>Te<sub>4</sub>.

## S5. Machine Learning Interatomic Potential Models Supported by UniMatSim

Table S2: Machine Learning Interatomic Potential Models Supported by UniMatSim

Model Name	Identifier	GitHub
CHGNet	PotentialModelType.CHGNET	<a href="https://github.com/CederGroupHub/chgnet">CederGroupHub/chgnet</a>
M3GNet	PotentialModelType.M3GNET	<a href="https://github.com/materialsvirtuallab/m3gnet">materialsvirtuallab/m3gnet</a>
MACE	PotentialModelType.MACE	<a href="https://github.com/ACEsuit/mace">ACEsuit/mace</a>
MatterSim	PotentialModelType.MATTERSIM	<a href="https://github.com/microsoft/mattersim">microsoft/mattersim</a>
SevenNet	PotentialModelType.SEVENNET	<a href="https://github.com/MDIL-SNU/SevenNet">MDIL-SNU/SevenNet</a>